Brain deletion of Serf2 shifts amyloid conformation in a mouse model

E. Stroo[1#], L. Janssen[1#*], O. Sin[1], W. Hogewerf[1], M. Koster[2], L. Harkema[2], S.A. Youssef[2,3], N. Beschorner[4], A.H.G. Wolters[5], B. Bakker[1], A. Thathiah[6,7], F. Foijer[1], B. van de Sluis[2], J. van Deursen[8], M. Jucker[4], A. de Bruin[2,3], E.A.A. Nollen[1*]

[1]European Research Institute for the Biology of Ageing, University of Groningen, University Medical Centre Groningen, The Netherlands

[2]Department of Biomolecular Health Sciences, Faculty of Veterinary Medicine, Utrecht University, The Netherlands

[3]Department of Pediatrics, Molecular Genetics Section, University of Groningen, University Medical Centre Groningen, The Netherlands

[4]Department of Cellular Neurology, Hertie-Institute for Clinical Brain Research, University of Tübingen, Tübingen, Germany.

[5]Department of Biomedical Sciences of Cells and Systems, University Medical Centre Groningen, The Netherlands

[6]VIB Center for the Biology of Disease, KU Leuven Center for Human Genetics, University of Leuven, Leuven, Belgium

[7] Department of Neurobiology, University of Pittsburgh Brain Institute, University of Pittsburgh School of Medicine, Pittsburgh, PA USA

[8]Mayo Clinic, United States of America

[#]These authors contributed equally

[*]Corresponding authors: l.l.s.janssen@umcg.nl or e.a.a.nollen@umcg.nl

Keywords: Small EDRK-rich factor 2, SERF, protein aggregation, amyloid-beta, amyloid polymorphisms

Highlights

- Loss of SERF2 slows embryonic development and causes perinatal lethality
- SERF2 affects proliferation in a cell-autonomous fashion
- Brain-specific *Serf2* knockout does not affect viability or Aβ production
- Brain deletion of *Serf2* shifts the amyloid conformation of Aβ

Abstract

Loss of protein homeostasis accelerates ageing and contributes to age-related brain diseases like Parkinson's and Alzheimer's diseases. Disease-specific proteins become aggregation-prone and form amyloid deposits that characterize disease, but the biological mechanisms driving their transition in cells and tissues are poorly understood. MOAG-4/SERF accelerates aggregation and toxicity of disease-related proteins in worm- and cell models. Whether MOAG-4/SERF affects amyloid pathology in brain, however, has remained unknown. Here we show that brain-specific knockout of SERF2 is viable and shifts aggregation in a mouse model for amyloid-beta aggregation. Without affecting amyloid-beta levels, knockout of SERF2 redirects its assembly into structurally and morphologically distinct amyloid fibrils and deposits. Our results show that SERF modifies the structural outcome of the aggregation process in mammalian brain. With structural polymorphisms recently being associated with disease severity and progression, our results may help to understand the molecular basis for structural diversity and find possibilities for structure-based interventions.

Introduction

Protein aggregation is a pathological hallmark shared by several age-related neurodegenerative diseases, such as Alzheimer (AD), Parkinson and Huntington disease. The amyloid-like aggregates that accumulate in each of these diseases are composed of disease-specific proteins, i.e., amyloid-beta (Aβ) and tau in AD[1–4], alpha-synuclein (α-Syn) in Parkinson disease[5] and Huntingtin (HTT) in Huntington disease[6]. While the exact molecular mechanisms underlying the disease pathology remain to be elucidated, genetic evidence indicates that these aggregation-prone proteins play a key role in the disease processes. In AD multiple causative mutations have been found in three genes: the amyloid precursor protein (*APP*)[7–15], presenilin-1 (*PSEN1*)[16–20] and presenilin-2 (*PSEN2*)[20–23] (for a full list of known AD-linked mutations see https://www.alzforum.org/mutations). The *APP* gene encodes the precursor protein from which Aβ is produced through sequential cleavage by a β- and γ-secretase. The *PSEN* genes encode the main catalytic subunit of the γ-secretase complex. The fact that all the causative mutations affect the production, length and/or structure of the Aβ peptides and are sufficient to cause the disease[7,8,17–23,9–16], is arguably the strongest piece of evidence for the involvement of Aβ in the disease process. Causative mutations generally affect the Aβ peptide in one of three ways: (i) an overall increase in Aβ production[9,24], (ii) a shift in the production of shorter variants, like $A\beta_{40,}$ to more aggregation-prone, longer variants, like $A\beta_{42}$ (or $A\beta_{43}$)[11,18,25–27], (iii) Aβ peptides with a modified core region, resulting in an increased propensity for aggregation[15,28–30]. Taken together, these mutations do not necessarily increase the amount of Aβ, but rather increase the likelihood of Aβ aggregation. Similarly, several mutations in the *SNCA* gene that have been linked to Parkinson disease have been shown to alter α-Syn aggregation[31–36]. In Huntington disease, any expansion of a polyglutamine stretch in the *HTT* gene that exceeds 36 repeats has been shown to facilitate HTT aggregation and cause the disease[37]. Hence, changes in the folding and aggregation of these disease proteins are believed to be at the basis of the observed pathology. In addition, there is increasing evidence that distinct structural variants exist between aggregates of the same disease protein and that these polymorphs are associated with varying degrees of toxicity[38–47] . For instance, recent studies with brain samples from human AD patients have shown that variations in the disease type and disease

progression correlate with the presence of structurally different aggregates and fibrils[40,41,48,49]. The knowledge that small changes in the structural conformation of these aggregates can have far-reaching effects on the disease manifestation could provide a new avenue for the development of therapeutics. Until now, most research into potential treatments of AD has focused on either reducing the overall amount of aggregating proteins or preventing aggregation, not modifying the aggregation process.

In a previous study, our group performed a genetic screen in *Caenorhabditis elegans* (*C. elegans*) and identified a small, intrinsically disordered protein of unknown function with the capacity to modify protein aggregation and to enhance the resulting toxicity of multiple disease-related, aggregation-prone proteins[50]. This peptide was dubbed *mo*difier of *ag*gregation-4 (MOAG-4) and was found to be an ortholog of two human genes: *Serf1A* and *Serf2*. Both SERF1A and SERF2 were shown to exacerbate protein aggregation and toxicity in human neuroblastoma and HEK293 cell lines as well[50]. *In vitro* assays with MOAG-4 and SERF1A have demonstrated that these proteins can specifically accelerate the aggregation kinetics of amyloidogenic proteins, but do not affect aggregation of non-amyloidogenic proteins[51,52]. For α-Syn, this amyloid-promoting effect has been shown to depend on the transient interaction of these positively-charged peptides with negatively-charged regions and the disruption intramolecular electrostatic interactions within the protein[51–53]. Removal of MOAG-4 or SERF from a biological system did not change the overall levels of the aggregation-prone proteins or activate chaperone pathways known to suppress aggregation[50]. Therefore, the reduced toxicity would appear to rely solely on the structural shift in the aggregation process[50,51]. In this study, we investigate whether the removal of SERF2 modifies the aggregation of Aβ in the biologically more complex environment of the mammalian brain.

Results

Full-body Serf2 KO results in developmental delay and perinatal lethality in mice

To establish the role of SERF2 *in vivo*, full-body *Serf2* knockout (KO) mice were generated (Figure S1A-C). During an initial cross, using the four homozygous *Serf2* KO animal (*Serf2*$^{-/-}$) and eight heterozygous *Serf2* KO animals (*Serf2*$^{+/-}$) we obtained, only one *Serf2*$^{-/-}$ survived the day of birth compared to 27 *Serf2*$^{+/-}$ and 96 *Serf2* wild-type (*Serf2*$^{+/+}$) mice (Supplemental Table 1). After backcrossing into C57BL/6J background, interbreeding of *Serf2*$^{+/-}$ animals did not result in any viable *Serf2*$^{-/-}$ mice at the time of weaning (Figure 1A,1B). To determine whether *Serf2*$^{-/-}$ mice died during fetal development, we examined the offspring at multiple developmental stages: embryonic day 13.5, 15.5 and 17.5. In all of the examined embryonic stages we observed the expected Mendelian ratio of genotypes, around 25 % *Serf2*$^{+/+}$ and *Serf2*$^{-/-}$ embryos and around 50 % *Serf2*$^{+/-}$ (Chi Square: E13.5 p=0.9672; E15.5 p= 0.4432; E17.5 p=0.7674) (Figure 1B). At birth (P0), all *Serf2*$^{-/-}$ displayed respiratory distress and the majority (5/7) died within 30 minutes of being born. At the time of weaning, the Mendelian ratio was maintained between the *Serf2*$^{+/+}$ and *Serf2*$^{+/-}$ animals, but no *Serf2*$^{-/-}$ mice survived until this stage (Chi Square: P22 p<0.0001) . Examination of *Serf2* mRNA expression at E13.5 showed a 50 % reduction for *Serf2*$^{+/-}$ and complete KO for *Serf2*$^{-/-}$ compared to *Serf2*$^{+/+}$ (One-way ANOVA: *Serf2*$^{+/-}$ and *Serf2*$^{-/-}$ vs *Serf2*$^{+/+}$ p_{Bon}<0.0001) (Figure 1C). A similar ratio in SERF2 expression was also observed on the protein level (Figure 1D). The *Serf1* mRNA levels were not affected by the change in *Serf2* levels, indicating there is no compensatory mechanism between these genes (One-way ANOVA: p=0.2403) (Figure 1C). Further analysis of the *Serf2*$^{-/-}$ embryonic phenotype revealed a reduction in embryo size of *Serf2*$^{-/-}$ compared to *Serf2*$^{+/+}$ and *Serf2*$^{+/-}$ from E15.5 until birth (Two-way ANOVA: E17.5 WT vs KO p_{bon}<0.05; P0 WT vs ko p_{Bon}<0.0001) (Figure 1E, S1D-E). No differences in size could be observed between *Serf2*$^{+/+}$ and *Serf2*$^{+/-}$ embryos during the embryonic stage leading up to birth (P0). Histological examination of various tissues revealed a developmental delay of approximately one to two days in the organs of E17.5 *Serf2*$^{-/-}$ embryos compared to the previous time points and standard embryonic development[54,55]. This was most prominently in the lungs, through reduced expansion of alveoli and augmented tissue density, and in

the kidneys, by the increased amount of mesenchyme between the tubules and glomeruli (Figure S1F). At the time of birth, the lungs of *Serf2*$^{-/-}$ pups displayed a significantly reduced saccular space (t-test: p= 0.0088) (Figure 1F), reflecting insufficient lung expansion and maturation. This partial fetal atelectasis seems to explain the observed respiratory distress and a likely cause of the perinatal lethality in *Serf2*$^{-/-}$ pups. Placental abnormalities have been shown to cause impaired transfer of nutrients and oxygen to the embryo, resulting in growth delays[56]. To exclude this as a potential cause, we examined the placenta at all three embryonic stages for microscopic lesions in the placental labyrinth or other changes. No genotype-related pathology could be found, indicating that absence of SERF2 in the embryo itself is responsible for the observed growth phenotype. This seems to be supported by the fact that CRISPR-induced *Serf2*$^{-/-}$ clones of HEK293T cells display a delay in proliferation (Figure S2A). Moreover, RNA sequencing analysis of mouse embryonic fibroblasts (MEF) isolated from E13.5 embryos showed a clear enrichment of GO-terms clustered around three closely related biological functions: cell cycle, cell proliferation and cell adhesion (Supplemental Figure S2A-B). Interestingly, in the cell cycle cluster we observe an overall upregulation of factors driving cell division and downregulation of growth arrest factors in *Serf2*$^{-/-}$ MEFs (Supplemental Table 2). This observation seems in line with a developmental delay phenotype in *Serf2*$^{-/-}$ mice, because it is known that cell proliferation is favored over differentiation in earlier stages of embryonic development compared to later stages[57]. Overall, the cell culture results point towards a cell-autonomous effect of SERF2 and suggest that loss of *Serf2* results in delayed growth. While our previous study also demonstrated a cell-autonomous function for moag-4, it did not show any effects of moag-4 deletion on the viability, life span or size of *C. elegans*[50]. All together, our results suggest that *Serf2* KO causes delayed maturation of certain organs at the time of birth resulting in death. Given the cell-autonomous nature of the effects of SERF2, we aimed to avoid these adverse effects by creating an organ-specific conditional KO model.

Brain-specific KO of Serf2 does not affect viability or the Aβ production pathway

To study the effect of *Serf2* KO on amyloid pathology in the brain, we circumvented the perinatal lethality of full-body *Serf2* KO mice by generating a brain-specific *Serf2* KO mouse model (*Serf2*$^{br-/-}$).

The conditional KO was obtained by combining our *Serf2*$^{flox/flox}$ mice with a *Sox1-Cre* model[58] (Figure S3A). SOX1 is one of the earliest transcription factors expressed in neuronal precursors of the ectoderm from embryonic day 7.5[59,60]. Consequently, the *Sox1* promotor was selected as a pan-neuronal driver of Recombinase cre expression to restrict homologous recombination to the central nervous system[58]. Analysis of *Serf2* expression on the mRNA and protein level in various organs confirmed brain-specific ablation of *Serf2* by *Sox1*-mediated *Cre* expression in our *Serf2*$^{flox/flox}$ mice (t-test WT vs *Serf2*$^{br-/-}$ brain: 1m p=0.0022; 3m p=0.00527) (Figure S3B-C). This conditional KO was crossed with the *APPPS1-21* amyloid (AM) model[61], which contains human transgenes for both APP with the Swedish KM670/671NL mutation and PSEN1 with the L66P mutation. From this cross we obtained four experimental groups: WT, *Serf2*$^{br-/-}$, AM and AM;*Serf2*$^{br-/-}$ (Figure 2A). Upon crossing of the *Serf2*$^{br-/-}$ with the amyloid model, we observed the expected Mendelian ratio for all the genotypes at P22, indicating that the viability is not significantly affected by brain-specific KO of *Serf2* (Chi Square: p= 0.37)(Supplemental Table 3). Based on the known progression of Aβ plaque pathology in the AM mice, we selected two age groups for further analysis: before (1 month) and after (3 months) Aβ plaque deposition (Figure 2B). Analysis of the *Serf2* mRNA levels in both age groups showed that *Serf2* expression was not altered by the plaque pathology and confirmed the KO in the *Serf2*$^{br-/-}$ and AM;*Serf2*$^{br-/-}$ mice. Some residual *Serf2* expression could be detected in the brains of the KO groups likely due to the presence of cells from non-neuronal lineage in the samples, e.g. cells from circulatory system (Two-way ANOVA: *Serf2*$^{br-/-}$ and AM;*Serf2*$^{br-/-}$ vs WT 1m p_{bon} <0.001; 3m p_{bon} <0.0001) (Figure 2C). These results were also confirmed on the protein level using western blot (Figure 2D). In accordance with the effects observed in the full-body *Serf2*$^{-/-}$ mice, the *Serf2*$^{br-/-}$ and the AM;*Serf2*$^{br-/-}$ mice did show a reduction in brain weight compared to WT in both age groups (Two-way ANOVA: *Serf2*$^{br-/-}$ vs WT both ages p_{bon}<0.01; AM;*Serf2*$^{br-/-}$ vs WT 1m p_{bon}<0.0001; 3m p_{bon}<0.001) (Figure 2E). While the weight reduction seems to be slightly more pronounced in AM;*Serf2*$^{br-/-}$ compared to *Serf2*$^{br-/-}$, AM by itself displayed no significant change in brain weight. This would indicate that *Serf2* ablation, *Cre* expression or a combination of both is most likely responsible for the difference in weight. However, AM mice may be more susceptible to this effect (Figure 2E). To distinguish between the effects of *Cre* expression and *Serf2* KO, we also examined the *Sox1-Cre*

mice[58] without floxed *Serf2* (*Cre*^{br}) and crossed them with *APPPS1-21*[61] without floxed *Serf2*. The *Cre*^{br} mice also showed a reduction in brain weight compared to the WT controls, which was more pronounced at 1 month (One-Way ANOVA: *Cre*^{br} vs WT 1m $p_{bon}<0.05$) (Figure S3D), but was overall less extensive than the reduction in *Serf2*$^{br-/-}$ animals (One-way ANOVA: *Cre*^{br} vs WT $p_{bon}<0.01$; AM;*Cre*^{br} vs WT $p_{bon}<0.001$) (Figure 2F). Together, this suggests that *Cre* expression is partially responsible for the observed decrease in brain size, particularly at 1 month of age. Due to ongoing brain maturation between 1 and 3 months, all groups show a significant increase in brain weight (Two-way Anova: Age $p<0.0001$), but this maturation appeared unaffected by *Serf2* KO. Moreover, the difference in brain weight between WT and *Serf2*$^{br-/-}$remained constant beyond the age of 3 months up to 11 months of age (Figure S3E). This suggests that the reduction in brain size takes place during specific stages of brain development, but that the continued development is not necessarily altered by these changes. Additional histological examination of the brains with hematoxylin-eosin staining revealed no difference in the cell density (Figure 2G), nor did we find any evidence of degeneration, apoptosis or necrosis. Apart from the overall reduction in weight, the brains showed no structural abnormalities and the tissue appeared healthy.

Next, we examined whether the brain KO of *Serf2* affected any of the key components in the Aβ aggregation process, like altering the levels of APP or the production of its cleavage products, $Aβ_{40}$ and $Aβ_{42}$. We determined the expression of human *APP* in WT, *Serf2*$^{br-/-}$, AM and AM;*Serf2*$^{br-/-}$ mice at both 1 and 3 months of age and observed no difference due to brain specific *Serf2* KO (t-test: 1m $p=0.9170$; 3m $p=0.9963$) (Figure 2H, data from WT, *Serf2*$^{br-/-}$ not included due to lack of APP construct and absence of signal). Western blot analysis confirmed there was also no difference in APP protein levels between AM and AM;*Serf2*$^{br-/-}$ (t-test: 1m $p= 0.1157$;3m $p=0.5908$) (Figure 2I and J). Further analysis of $Aβ_{40}$ (Two-way ANOVA: Genotype $p=0.8841$; Age $p<0.0001$;Interaction $p=0.8841$) (Figure 2K) and $Aβ_{42}$ (Two-way ANOVA: Genotype $p=0.7006$; Age $p<0.0001$;Interaction $p=0.6522$) (Figure 2L) showed an increase in concentration between 1 and 3 months, but this was the same in both AM and AM;*Serf2*$^{br-/-}$. Given the variability in the Aβ concentrations at 3 months and the fact that the ratio between these two peptides is known to affect the aggregation process, we also

investigated the correlation between these two Aβ levels (Figure 2M). This analysis showed that mice with a high $A\beta_{42}$ concentration display a similarly high $A\beta_{40}$ level, maintaining a comparable $A\beta_{40}$ /$A\beta_{42}$ ratio for both AM and AM;*Serf2*$^{br-/-}$ animals. Taken together, this data suggests that SERF2 does not affect the levels of APP and its cleavage products, $A\beta_{40}$ and $A\beta_{42}$. These findings are in accordance with the previously observed effects of MOAG-4 on the aggregation of polyglutamine, Aβ and αSyn in *C. elegans*, which modifies the aggregation process without changing the overall levels of these aggregation-prone proteins[50]. While the difference in brain size is definitely a factor to be considered during further analysis, given the fact that we observed no obvious changes in the overall health, continued development and APP processing pathway of these brain-specific *Serf2* KO mice, we proceeded with our analysis of Aβ pathology in these animals.

Serf2 KO alters the amount of Aβ deposition in the brain

We next investigated whether SERF2 affects the Aβ aggregation by performing immunohistological analysis of the Aβ plaque pathology. Initially, we performed a general Aβ staining using the 6E10 antibody. In accordance with the known progression of Aβ plaque pathology in the amyloid model, we only found extracellular deposits in the 3-month-old AM and AM;*Serf2*$^{br-/-}$ mice. As expected, most plaques were found in the cortex, with some pathology beginning to spread to the hippocampus as well (Figure S4). Microscopic inspection of the Aβ deposits revealed a broad range of sizes with a wide variety in staining intensity and patterns, but we found no clear morphological differences between the plaque population found in AM and AM;*Serf2*$^{br-/-}$ (Figure 3A, S4). Quantification of the 6E10-positive deposits showed a slight increase in AM;*Serf2*$^{br-/-}$ compared to AM, but this just failed to reach statistical significance in the Bonferroni corrected post-hoc comparison (Two-way ANOVA: all 3m non-AM vs AM groups p_{bon} <0.0001; AM vs AM;*Serf2*$^{br-/-}$ p_{bon} =0.063)(Figure 3B). Given the high variability in plaque load between animals within the same experimental group, we examined whether this variability reflected the previously observed variation in Aβ levels. Unsurprisingly, animals with higher levels of $A\beta_{40}$ (Figure 3C) and $A\beta_{42}$ (Figure 3D) displayed a higher overall plaque load in both groups. More interestingly, our linear regression analysis revealed that AM;*Serf2*$^{br-/-}$ mice tend to have a significantly higher plaque load than AM mice with similar Aβ levels (Supplemental

Table 4). A second general Aβ stain with the W0-2 antibody displayed a similar slight increase in the amount of plaque deposits in AM;*Serf2*$^{br-/-}$ at 3 months (Two-way ANOVA: all 3m non-AM vs AM groups p_{bon} <0.0001; AM vs AM;*Serf2*$^{br-/-}$ p_{bon} =0.101) (Figure 3E). In fact, a comparison between the 6E10 and the W0-2 staining in individual animals confirmed the similarity between both staining patterns at 3 months (Figure 3F, S5, Supplemental Table S3). Interestingly, our detection algorithm also picked up a small increase in the counts of W0-2-positive foci in the 1 month AM;*Serf2*$^{br-/-}$ group (Two-way ANOVA: 1m WT vs AM;*Serf2*$^{br-/-}$ p_{bon} =0.088 ; *Serf2*$^{br-/-}$ vs AM;*Serf2*$^{br-/-}$ p_{bon} =0.081; AM vs AM;*Serf2*$^{br-/-}$ p_{bon} =0.127; all other comparisons p_{bon} >0.999) (Figure 3E). Closer examination of the microscopic images revealed the identified spots were not extracellular plaques, but were the result of increased levels of W0-2-positive intracellular staining in AM;*Serf2*$^{br-/-}$ (Figure S7A). Some low level intracellular W0-2 and 6E10 staining could also be observed in the other 1-month-old AM mice, but not to the extent that it was picked up by the detection algorithm (Figure S7A-B). This would suggest that the deletion of *Serf2* already alters the intracellular accumulation of Aβ prior to plaque deposition. Overall, these results indicate that the presence of SERF2 is indeed able to modify Aβ aggregation in the mouse brain.

SERF2 deficiency changes the proportion of ThS-positive cores, but not the immunoreactivity of deposits

To investigate if SERF2 also affected the amount of Thioflavin-positive fibrils, we performed Thioflavin-S (ThS) staining. Here, we again observed a large variety in the amount of ThS-positive plaques between individual animals, but we found no mean difference between AM and AM;*Serf2*$^{br-/-}$ mice (Two-way ANOVA: all 3m non-AM vs AM groups p_{bon} <0.001) (Figure 3G). However, further analysis of the correlation between Aβ levels and the amount of ThS-positive plaques revealed that AM mice showed a positive correlation similar to the general Aβ stainings, while AM;*Serf2*$^{br-/-}$ mice displayed an inverse relationship (Figure 3H, 3I, Supplemental Table S3). Consequently, a general increase in Aβ deposits does not equate to an increase in amyloid deposition in AM;*Serf2*$^{br-/-}$ mice, as it does in AM mice (Figure 3J), further demonstrating a change in the amyloid formation in *Serf2* KO mice. In addition, we investigated microglia activation and whether we could detect a change in the

gliosis associated with Aβ plaques. Staining for Iba1 showed a slight increase in the AM;*Serf2*$^{br-/-}$ mice compared to AM (Two-way ANOVA: 3m non-AM groups vs AM p_{bon} <0.01; non-AM groups vs AM;*Serf2*$^{br-/-}$ p_{bon} <0.0001; AM vs AM;*Serf2*$^{br-/-}$ p_{bon} <0.01) (Figure 3K), similar to what was observed with the 6E10 staining (Figure 3B). We therefore examined if this increase was simply related to the increase in Aβ deposits or if AM;*Serf2*$^{br-/-}$ also displayed a different immune response to plaques compared to AM. Our analysis revealed a similar correlation between 6E10-positive deposits and immune response for AM and AM;*Serf2*$^{br-/-}$ mice, suggesting the deposits evoked a similar immune response in both groups(Figure S6A, Supplemental Table S3).

Knockout of Serf2 changes the plaque composition and fibril structure

Given the differences in the reactivity of the Aβ deposits between the various stains, we decided to explore the composition within the individual plaques in greater detail. To this end, we made use of two luminescent conjugated oligothiophenes (LCO), qFTAA (quadro-formylthiophene acetic acid) and hFTAA (hepta-formylthiophene acetic acid). These LCOs are small hydrophobic ligands with a high affinity for binding distinct types of amyloids and can easily be distinguished from each other based on their spectral properties[62]. The smallest of the two molecules, qFTAA, is characterized by a peak in its emission spectrum around 500 nm and has been shown to stain compact, multifilament fibril structures, coinciding with ThT and Congo red staining[62–64]. Whereas hFTAA emits in the yellow to red range with a peak around 600 nm and is capable of staining prefibrillar (non-thioflavinophilic) and single fibril aggregates found during the lag-phase of in vitro ThT kinetics (Figure 4A). The prefibrillar aggregates were shown to be stained with 6E10, but not Congo red, ThT or qFTAA[62–64]. Previous studies have shown that by combining LCO dyes it is possible to uncover structural differences in plaque composition[49,64,65]. We performed confocal spectral imaging of randomly selected plaques in 3-month-old AM and AM;*Serf2*$^{br-/-}$ mice after double staining with both LCOs and determined the ratio of the light intensity emitted at 502nm and 588nm as a measure for the relative amounts of fibrillar and prefibrillar aggregates within the individual plaques. An exploratory frequency analysis of the intensity ratios found in both groups revealed a three-peak pattern in which the middle peak was similarly represented in both groups (Figure 4B, green area). The first peak,

however, was predominantly found in AM mice (Figure 4B, red area), while the third peak was mainly detected in AM;*Serf2*$^{br-/-}$ (Figure 4B, blue area). This shift in ratio was also reflected by a significant difference in the average intensity ratio between AM and AM;*Serf2*$^{br-/-}$ (t-test $p<0.001$) (Figure 4C). This increase in intensity ratio could not be observed in AM;*Cre*^{br} mice (t-test $p=0.6047$) (Figure 4C, insert), indicating that this effect is caused by the *Serf2* KO and unrelated to *Cre* expression. Given the fact that AM;*Cre*^{br} animals also show a decrease in brain weight without a change in LCO staining, this would also suggest that the weight reduction is not a factor in these results. Although, as the change in brain weight is more pronounced in *Serf2*$^{br-/-}$ animals, we cannot completely exclude this as a potential contributing factor. Next, we examined if the change in the intensity ratio correlated with the slight increase in 6E10-positive deposits we observed in AM;*Serf2*$^{br-/-}$ (Figure 4D). However, the higher average intensity ratio in AM;*Serf2*$^{br-/-}$ mice was not related to this general plaque load nor the number of W0-2- or ThS-positive deposits (Figure S6B, S6C). Further microscopic analysis of low intensity ratio deposits from AM mice showed a plaque with a qFTAA- and hFTAA-positive core and a border that was only stained by hFTAA (Figure 4E, left panels). The high intensity ratio deposits from AM;*Serf2*$^{br-/-}$ mice, on the other hand, revealed a qFTAA-positive core, but virtually no hFTAA-staining (Figure 4E, right panels), demonstrating the difference in plaque composition reflected by the shift in LCO intensity ratios. Additionally, we visualized the global fibrillar structure of the plaques on a nanometer scale using high resolution, scanning transmission electron microscopy (STEM). Overall, STEM images of plaques from AM;*Serf2*$^{br-/-}$ tended to show more condensed plaques composed of short, thick and densely packed bundles of fibers with little space in between (Figure 4F, right panels). In the AM mice, however, the plaques we observed displayed more loosely packed fibrils (Figure 4F, left panels). Taken together, these findings suggest *Serf2* KO in mice leads to a shift in the Aβ aggregation process, resulting in an altered structural composition of the plaques.

Discussion

Previous studies identified MOAG-4 and its human orthologs SERF1A and SERF2 and their potential to modify the aggregation of amyloidogenic proteins. While the exact endogenous biological function of these peptides remains unclear, a recent study has provided evidence for RNA-binding properties of

SERF1A through a region which is highly conserved in MOAG-4 and SERF2[66]. In this study, we have demonstrated in cells and mice that SERF2 provides a growth advantage during development. The absence of SERF2 or MOAG-4 in itself does not appear to be lethal in cells, worms or the brain-specific KO mice. Therefore, we postulate that the observed perinatal lethality in the full-body KO mice is a secondary effect of the delay in growth due to insufficient maturation of certain organs at birth. This appears to be supported by the fact that some pups survived the initial minutes after birth and incomplete penetrance of the lethality in the earliest generations with mixed genetic background. The 129SV genetic background present in these mice is known to have a gestation period that is on average around one day longer than C57/Bl6J mice[67], which could result in improved lung maturation. While the exact function of SERF2 remains unknown, we propose its effects on growth and development are most likely caused through one of two mechanisms: either SERF2 facilitates cell proliferation or it protects cells from stressors that create an unfavorable environment for cell division. In the latter case, we would expect to see an upregulation of stress pathways or cell cycle arrest proteins inhibiting the cell cycle in *Serf2*$^{-/-}$ cells. Interestingly, the RNA seq analysis of the MEFs from our *Serf2*$^{-/-}$ mice showed the exact opposite. Cell cycle driving factors were upregulated (e.g. cyclins). Whereas, stress signaling and cell cycle inhibiting factors were downregulated (e.g. GADD45 and GAS1). Thus, the *Serf2*$^{-/-}$ cells actually displayed an increased stimulation of cell proliferation mechanisms, which would fit with cells from earlier stages of embryonic development. This would suggest the first mechanism, with a beneficial role for SERF2 in the efficient execution of cell proliferation, as the most likely explanation for the observed growth effect. Furthermore, an increase in cellular stress would most likely result in decreased health and fitness. However, *moag-4* deletion worms showed no changes in life span compared to controls[50] and, apart from the initial growth deficit, the tissues of *Serf2* KO mice appeared healthy and continued to develop similarly to controls after birth. A recent study showed SERF1a might play a role as an RNA-organizing protein, which localizes to membraneless nuclear organelles, like the nucleolus, under normal physiological conditions. However, under stress conditions, it was shown to migrate to the cytoplasm, where it could drive amyloid toxicity.[66] While there was no compensatory upregulation of SERF1 in response to SERF2 KO and a similar mode of action remains to be demonstrated for SERF2, the structural

335 homology of the two proteins would suggest a comparable function. Given the importance of
336 nucleolar disassembly and reassembly in cell cycle control[68,69], an RNA-organizing function could
337 explain how SERF2 facilitates cell proliferation. This developmental role would have limited
338 biological importance in non-proliferating, differentiated cells, like the brain's neurons or the cells of
339 adult *C. elegans*, and might also explain why we saw no adverse effects in the *moag-4* deletion worms
340 or our adult *Serf2*$^{br-/-}$ mice. While a reduced biological importance of SERF2 later in life could prove
341 interesting with regard to the treatment of age-related neurodegenerative disorders, further exploration
342 of SERF2's endogenous function and how it evolves with ageing will be needed to fully assess this
343 mechanism's therapeutic potential.

344 In this study, we confirmed the ability of SERF2 to modify the Aβ pathology *in vivo* in a mouse model
345 without changing the overall Aβ levels. We showed that mice lacking SERF2 were more prone to
346 form Aβ deposits and that the composition of these deposits was structurally different. In AM mice
347 higher levels of Aβ result in an increase in the numbers of Aβ deposits as well as an increase in the
348 number of ThS-positive deposits. AM;*Serf2*$^{br-/-}$ mice, on the other hand, also show an increase in Aβ
349 deposits, but this did not lead to higher numbers of ThS-positive plaques, indicating an altered
350 dynamic for amyloid formation. These findings were further corroborated by the LCO spectra, which
351 revealed that the plaques in AM;*Serf2*$^{br-/-}$ mice have a different conformation of pre-fibrillar and
352 fibrillar Aβ compared to AM mice. Finally, STEM imaging also confirmed a globally altered structure
353 of the amyloid fibrils in the plaques. Amyloid fibrils are formed through a nucleated self-assembly
354 process characterized by a structural conformation to a β-strand secondary structure and the formation
355 of a critical nucleus during the initial oligomerization. The nuclei act as seeds from which the fibrils
356 grow and have been shown to propagate a specific fibril structure[41,70]. In vitro kinetic assays with
357 SERF and MOAG-4 have shown that these peptides accelerate aggregation by acting on the nucleation
358 phase[51–53,71]. Recently, we have shown that SERF2 is equally capable to drive amyloid formation of α-
359 Syn and Aβ *in vitro* through a conserved, positively charged region[72]. Meanwhile, another study has
360 demonstrated that binding of the intrinsically disordered protein yeast SERF to α-Syn and Aβ results
361 in fuzzy complexes with heterogeneous structural conformations that are more extended in

nature[71]. For α-Syn, the disruption of intra-molecular electrostatic interactions by the positively charged region of MOAG-4/SERF1 was found to expose an amyloid nucleation site[52,53]. Intra-molecular electrostatic interactions have also been proven to play a part in the dynamics and structure of the Aβ monomer folding, which is at the basis of nucleus formation. In fact, several of the familial AD mutations located within the Aβ sequence and reported not to affect the Aβ levels, appear to exert their effects by modifying the intra-molecular interactions and monomer folding[30,73–75]. These single amino acid modifications in the Aβ sequences also result in alterations in the aggregation kinetics, fibril structure and aggregate toxicity in *in vitro* studies[29,76,77]. Moreover, patients and mouse models with these mutations show differences in the localization of Aβ accumulation and deposition, as well as differences in its structure, giving rise to specific disease phenotypes. For instance, while some mutations result in increased Aβ deposition and altered plaque structure, other mutations at the same location result in cerebral amyloid angiopathy with Aβ deposition in blood vessels rather than the brain parenchyma or even an absence of extracellular Aβ deposition[15,28,82,83,30,65,73,77–81]. In addition, some of these mutants showed increased intracellular Aβ accumulation which differed in structure-specific staining characteristics[83–85]. The differences in Aβ pathology between these mutants seem to display some similarities to the changes we observed between our AM and AM;*Serf2*$^{br-/-}$ mice. Together with the *in vitro* findings about the mechanism of SERF2 interaction with aggregation-prone proteins, this would appear to suggest modulation of intra-molecular interactions and altered nucleation as the mechanism for SERF2's effect on aggregation and amyloid formation in our mice. Interestingly, there is increasing evidence that qualitative, structural properties may be more related to toxicity than the quantity of aggregates and deposits. Recent studies have provided increasing evidence that structural polymorphs are associated with differences in toxicity and different clinical phenotypes in sporadic and familial cases[40,41,47–49]. One recent study demonstrated that these structural conformations of distinct disease phenotypes could also be detected by differences in the LCO spectra of the plaques and that these spectral properties could, at least partially, be transmitted to a mouse model through seeding[49]. While the effect of familial mutations on the formation of distinct polymorphs has already been explored by others[49,84–86], our study provides the first evidence of a single endogenous factor, separate from Aβ and its production pathway, contributing to a structural

shift of amyloid pathology in a mammalian system. Further research will be needed to elucidate the exact structural changes at an atomic level and if they affect toxicity and disease progression similarly to what was previously observed in *C. elegans*. This will provide new insights into the structural properties and diversity of disease-protein aggregation, contributing to a better understanding of the variability in disease manifestation and open up previously unexplored avenues for therapeutic research.

Materials and methods

Animals

Serf2 knockout mice were generated by introducing *loxP* sites in the *Serf2* gene on either side of exon 2, in accordance with the 'knockout-first' allele design as described by Skarnes and colleagues[87]. Full-body *Serf2* knockout mice were obtained by crossing these floxed mice with 129SV mice expressing *Cre* under the *Hprt* promoter, resulting in the removal of exon 2 by *Cre*-mediated recombination (Figure S1A). Subsequently, these mice with mixed background were backcrossed at least 6 times to a C57Bl/6J background. Homozygous and heterozygous full-body *Serf2* knockout mice were examined with their wild-type littermates at embryonic day 13.5, 15.5 and 17.5, as well as at the day of birth (P0) and day of weaning (P22).

Heterozygous *Sox1-Cre* mice[58] were backcrossed at least 8 times to a C57BL/6J background. These animals were also used as controls to differentiate between effects of *Cre* expression and Serf2 knockout. To generate the conditional *Serf2* knockout mice, the floxed mice were first crossed with Tg(ACTFLPe)9205Dym (Jackson#003800) mice to flip the FRT site and remove the lacZ and neo cassette. Subsequently, these mice were backcrossed at least 6 times to a C57BL/6J background. Finally, the resulting homozygous $Serf2^{flox/flox}$ mice were crossed with the backcrossed *Sox1-Cre* mice, to obtain the brain-specific *Serf2* knockout mice (Figure S3A). The conditional *Serf2* knockout mice were crossed with the APPPS1-21 transgenic mice (APP (KM670/671NL)/PS1(L166P), Rottenburg, Germany) [61]. A final cross between heterozygous APPPS1-21; $Serf2^{flox/flox}$ and heterozygous *Sox1-Cre*; $Serf2^{flox/flox}$ resulted in four experimental groups of $Serf2^{flox/flox}$ mice: $Sox1\text{-}Cre^{-/-}$; APPPS1-$21^{-/-}$ (WT),

416 *Sox1-Cre*$^{+/-}$; APPPS1-21$^{-/-}$ (*Serf2*$^{br-/-}$), *Sox1-Cre*$^{-/-}$; APPPS1-21$^{+/-}$ (AM) and *Sox1-Cre*$^{+/-}$; APPPS1-21$^{+/-}$
417 (AM;*Serf2*$^{br-/-}$) (Figure 2A). All experimental groups were tested at 1 month or 3 months of age.

418 All experiments were approved by the Institutional Animal Care and Use Committee of the University
419 of Groningen (Groningen, The Netherlands). All mice were maintained on a C57BL/6J background
420 and housed in a 12:12 hour light/dark cycle and the animals had ad libitum access to food and water.
421 Genotyping of embryos was performed using tail and yolk sac biopsies. Otherwise, ear biopsies were
422 used. DNA was purified using prepGEM® Tissue kit according to a protocol adapted from the
423 manufacturer (ZYGEPTI0500, ZyGEM, VWR International BV) and subjected to PCR using the
424 primers listed in Supplemental Table S5. Mice were terminated through CO_2-inhalation and cervical
425 dislocation for subsequent tissue collection.

426 *Embryo processing and histochemistry*

427 Embryos were fixed in 4 % formalin (Kinipath) for a minimum of 24 hours at room temperature. For
428 the pathological analysis, the embryos and their placenta were bisected longitudinally and embedded
429 in paraffin. Using the microm HM 340E (Thermo Scientific) 4 µm sections were cut for the
430 hematoxylin-eosin (HE) staining. The HE sections were incubated at 60 °C for 15 minutes. Next,
431 sections were deparaffinized and rehydrated in xylene (2x), 100 % alcohol (2x), 96 % alcohol, 70 %
432 alcohol and water. HE staining was performed by incubation with hematoxylin for 4 minutes, water
433 for 10 minutes, eosin for 1 minute and water for 10 seconds. After staining all sections were
434 dehydrated in 70 % alcohol, 96 % alcohol, 100 % alcohol (2x) and xylene (2x).

435 *Brain processing*

436 Upon termination, all brains were collected and weighed. From each experimental group three whole
437 brains were collected for HE staining according to the protocol described under embryo processing.
438 HE-stained sections were scanned with the TissueFAXs microscope using 20X objective. Images were
439 processed for nuclei counts using Histoquest software. The remaining brains were divided sagittally.
440 The left hemibrain was prepared for histochemistry and fixed in 4 % paraformaldehyde (PFA) for 48

hours at room temperature on a shaker. Next, the brains were placed in 30 % sucrose for approximately 12 hours. Afterwards, the excess sucrose was removed and hemibrains were frozen in molds with Tissue Tek O.C.T. compound (Sakura, The Netherlands) on dry ice. The right hemibrain was snap frozen in liquid nitrogen and stored at -80°C. This tissue was homogenized using a liquid nitrogen cooled mortar for subsequent protein and RNA analysis.

Quantitative RT-PCR

Total RNA was extracted from snap frozen tissue using TRIzol Reagent (Life Technologies) according to the manufacturers' description. Total RNA quality and concentration were assessed using a NanoDrop 2000 spectrophotometer (Thermo Scientific/Isogen Life Science). cDNA was made from 1,5 µg total RNA with a RevertAid H Minus First Strand cDNA Synthesis kit (Thermo Scientific) using random hexamer primers. Quantitative real-time PCR was performed using a Roche LightCycler 480 Instrument II (Roche Diagnostics) with SYBR green dye (Bio-Rad Laboratories) to detect DNA amplification. Relative transcript levels were quantitated using a standard curve of pooled cDNA solutions. Expression levels were normalized to β-Actin or 18S mRNA levels. The primers for Quantitative PCR used are listed in Supplemental Table S5.

Western Blot analysis

For SERF2 analysis tissues were homogenized in RIPA buffer (50 mM Tris pH 8, 150 mM NaCl, 5mM EDTA, 0.5 % SDS, 0.5 % SDO, 1 % NP-40) with protease inhibitor cocktail (Roche) and incubated on ice for 1 hour, spun down at 13,300 rpm for 30 minutes at 4 °C and the supernatant was collected. Protein measurements were performed using a BCA kit (Pierce) and 150 µg was loaded on a 10-20 % tris/tricine SDS-page gels (Bio-Rad Laboratories) and blotted onto 0,2 µm nitrocellulose membrane (Bio-Rad Laboratories). Membranes were incubated overnight with SERF2 (1/1500, Protein tech) or Actin (1/10 000, MP biomedicals) antibody. Next, the membranes were incubated with anti-mouse or –rabbit secondary antibodies tagged with horseradish peroxidase (1/10 000, Bio-Rad Laboratories) for one hour at room temperature and visualized by chemiluminescence (Amersham ECL prime western blotting detection reagent, VWR).

RNA sequencing

RNA sequencing analysis was performed on three MEF cell lines from *Serf2*$^{-/-}$ mice and four *Serf2*$^{+/+}$ littermate controls. Total RNA was isolated from MEFs using the Qiagen RNeasy isolation kit. Integrity of the RNA based on RIN scores as determined by a Bioanalyzer (Agilent). RNA-sequencing libraries were prepared using TruSeq Stranded Total RNA with Ribo-Zero Human/Mouse/Rat (RS-122-2201; Illumina, CA, USA) according to manufacturers' protocol. Pooled libraries were sequenced on an Illumina HiSeq 2500 (single-end 50 bp). Reads were aligned to the mouse reference genome (mm10) using a splicing-aware aligner (StarAligner). Aligned reads were normalized to fragments per million (FPM), excluding low abundance genes (mean FPM>1 in at least two samples). The raw count data were pre-processed using the programming language R (3.4.0) [R Core Team, 2016, available online at: www.r-project.org], the program RStudio (1.0.143) [RStudio Team, 2016, available online at: http://www.rstudio.com/] and the EdgeR package (3.18.0)(Robinson et al., 2010). Genes that displayed FPM value >1 in at least two libraries were retained, resulting in a list of 12,808 genes for differential analysis. Differentially expressed (DE) genes between the *Serf2*$^{+/+}$ and *Serf2*$^{-/-}$ MEFs were identified using the EdgeR general linear model approach. After statistical correction for multiple comparisons with the "false discovery rate" (FDR) method (FDR<0.05), a list of 738 DE genes was obtained. DAVID (6.8) was used to perform functional annotation analyses on this gene list and to identify significantly enriched gene ontology (GO) terms [using GOTERM_BP_DIRECT] [88,89]. The connectivity between the enriched GO terms was further examined by determining the amount of associated genes found (AGF) that were shared between two GO terms. The most significant relationships (where a GO term shared > 25 % of the AGF) were mapped in a network using the igraph package (1.0.1). The color of the edges reflects the major node, with the largest amount of AGF, in each relationship. The weight of the edges was determined by the percentage of AGF shared by the minor node in the relationship. We defined three clusters of GO-terms, where multiple minor GO-terms connected to one or two central, major GO-terms . Minor GO-terms were always clustered with the major GO-term with whom they shared the strongest connection. One GO term, positive

493 regulation of the apoptotic process, showed no direct relation with one of the major GO-terms and was
494 therefore assigned to the only cluster it had a significant connection with (Figure S2A-B).

495 *ELISA*

496 The ELISA experiments were performed as described previously[90]. Briefly, the frozen brain samples
497 were homogenized in tissue protein extraction reagent (Pierce) supplemented with complete protease
498 inhibitors (Roche), and centrifuged for 1 hour at 430 000 g at 4 °C. The supernatant was used for
499 ELISA. The $A\beta_{40}$ and $A\beta_{42}$ levels were determined by standard sandwich ELISAs using end-specific
500 antibodies (Janssen Pharmaceutical), and the monoclonal JRFcAβ_{40}/28 and JRFcAβ_{42}/26 antibodies as
501 the capture antibodies. Horseradish peroxidase conjugated JRFAβN/25 or JRFAβN/25 were used as
502 the detection antibodies for, respectively, human Aβ or murine Aβ. Samples were loaded in triplicate
503 for each ELISA. The ELISAs were performed in triplicate for the 3-month-old animals and in
504 duplicate for the 1-month-old animals.

505 *Brain immunohistochemistry*

506 To evaluate Aβ-related pathology, the brain was cut in 30 µm thick serial cryostat sections. A series of
507 sections was selected with 300 µm spacing between individual sections and blind-coded, 6 per mouse
508 for the 6E10 and Iba1 antibody and 3 per mouse for W02. Sections were fixed in 4 % PFA for 10
509 minutes, followed by 20 minutes antigen retrieval in citrate acid (pH 6.0) and 30 minutes in 1 % H_2O_2
510 in methanol. Next the sections were incubated for 1 hour in 10 % goat or donkey serum, depending on
511 the secondary antibody, and immunolabeled overnight with antibodies against Aβ, and Iba1
512 (Supplemental Table S6). The sections were washed and incubated with the complementary
513 biotinylated secondary antibody (1/500, Jackson Immunoresearch) for 2 hours. Next, sections were
514 incubated in ABC complex and reacted with diamino-benzidine (0.5 mg/ml H2O with 0.01 % H_2O_2).
515 The stained sections were scanned with the TissueFAXs microscope using 20X objective. All images
516 were analyzed using the Fiji platform of the ImageJ software[91]. For unbiased feature detection we used
517 a single automated script with optimized threshold method and parameters for the complete image set
518 of each staining method.

519 *Thioflavin-S Staining*

520 A 300 µm-spaced series of three blind-coded 30 µm sections were fixed in 4 % PFA for 10 min,
521 followed by incubation in 0.25 % potassium permanganate solution for 15 min, and a bleaching step
522 with 1 % potassium metabisulfite/1 % oxalic acid for 5 min, incubation with 0.02 % Thioflavin-S
523 solution in 50 % ethanol (Sigma T1892) for 8 minutes, rinsed with water between every step. Finally
524 the sections were incubated with 1 µl/ml DAPI. The sections were analyzed as described for the
525 immunostained sections. Stained sections were scanned with the TissueFAXs microscope using 20X
526 objective. Images were processed using Tissuequest software, selecting the cortex for automated
527 analyses.

528 *Luminescent conjugated oligothiophene (LCO) staining*

529 For the Luminescent conjugated oligothiophenes (LCO) stainings, two different LCO variants,
530 qFTAA (quadro-formyl thiophene acetic acid) and hFTAA (hepta-formyl thiophene acetic acid) were
531 used. Blind-coded 30 µm sections were double-stained with qFTAA and hFTAA (2.4 µM qFTAA and
532 0.77 µM hFTAA in PBS) similar to a previous description (Nyström et al., 2013). Sections were
533 incubated for 30 minutes in the dark at room temperature. Stainings were analyzed on the Zeiss LSM
534 510 META confocal microscope equipped with an argon 458 nm laser (Carl Zeiss MicroImaging
535 GmbH, Jena, Germany). An 40x objective (oil-immersion, 1.3 NA, Zeiss) was used for spectral
536 imaging of the Aβ deposits. Stacked images were acquired every 10 nm in the emission spectrum
537 between 470 to 695 nm. Locations were selected randomly from the plaque containing regions of the
538 temporal, frontal and occipital cortex. Images were analyzed using Fiji (Schindelin et al., 2012, 2015)
539 and standard computer algorithms to provide a reproducible, unbiased detection of the plaques. First,
540 the stacks of images across the different wavelengths of the spectrum were combined into one image
541 using the Z-projection sum. A threshold was applied to the resulting image using the "Triangle dark"
542 algorithm to automatically identify and delineate the plaques. Partial plaques on the edge of the images
543 and particles smaller than 25 μm^2 were excluded. These settings allowed us to detect over 98 % of all
544 the plaques in the images. The missed plaques were either too small or too low in intensity to be

accurately distinguished from the background. Incorrectly identified particles due to (lipofuscin) auto fluorescence were readily identified based on their wavelength intensity profile and visual inspection and were also excluded from the analysis. We identified between 17-25 plaques in each animal for the spectral intensity measurements. The ratio of the intensity of emitted light at the blue-shifted portion (502 nm) and red-shifted peak (588 nm) was used as a parameter for spectral distinction of different Aβ deposits. These peaks of the spectra were selected to maximize the spectral distinction.

Large-scale STEM (nanotomy)

The scanning transmission electron microscopy (STEM) experiments were adapted from previously described experiments (Kuipers et al., 2015). Briefly, paraffin embedded cortical sections of AM and AM;*Serf2*$^{br-/-}$ were deparaffinized and postfixed with 1 % osmium tetroxide/1.5 % potassium ferrocyanide in 0.1 M sodium cacodylate, dehydrated through ethanol and embedded in EPON (Serva) using a tissue processor (Leica EM TP 709202). Ultrathin sections (80 nm) were cut using the Leica uc7 ultramicrotome and collected on formvar coated cupper grids (electron microscopy sciences, Hatfield, Pennsylvania). A large area scan using Scanning Transmission Detection was made using a Zeiss supra55 SEM with Atlas. STEM detection with a four quadrant STEM detector was used in inverted darkfield mode, at 28 kV with 30 µm aperture at 3.5 mm working distance. All images were recorded at the same scan speed (cycle time 1.5 minute at 3072×2304 pixels). Contrast and brightness were set based on a live histogram. High resolution large-scale STEM images at 2.5 nm pixel size were generated with the external scan generator ATLAS (Fibics, Canada), individual tiles were stitched in VE viewer (Fibics, Canada), exported as a html-file and uploaded to the website www.nanotomy.org.

Cell culture

Mouse embryonic fibroblasts (MEFs) were isolated from *Serf2*$^{+/+}$, *Serf2*$^{+/-}$ and *Serf2*$^{-/-}$ E13.5 embryos. MEFs were cultured in T75 culture flasks (Greiner Bio-One, 658175), high–glucose Dulbecco's modified Eagle's medium (Gibco), supplemented with 10% fetal bovine serum (Sigma 12133C), 1 %

penicillin/streptomycin (Gibco), non-essential amino acids (Gibco) and β-mercaptoethanol at 37°C, 5 % CO_2 and 3 % O_2. E13.5 embryos. Wild-type HEK293T and two independent clonal lines of CRISPR *Serf2* KO mutant HEK 293T cells were cultured in Dulbecco's Modified Eagle Medium (DMEM, Gibco; high glucose, pyruvate, 41966052), supplemented with 10 % Bovine Cow Serum (BCS; Sigma 12133C) and 1 % Penicillin/Streptomycin (Gibco; 10 000 U/mL, 15140122), at 37 °C, 5 % CO_2. For passaging of cells, 0.05 % Trypsin-EDTA (1X), Phenol Red (Invitrogen; 25300-054) was used. Regular mycoplasma tests were performed.

Cell proliferation assay

For the proliferation assay, 200 000 cells of each cell line were plated in triplicate in a standard 12-well plate and incubated inside the IncuCyte Zoom Live-Cell Imaging System (Essen Bioscience) for over 100 hours. The Incucyte system captured phase contrast images with a 10X magnification every 2 hours at nine distinct locations in each well to determine average confluency as a measure of cell growth. The quantification was performed using the IncuCyte Zoom software. The growth experiment was repeated three times. The confluency data of each experiment was normalized by min-max scaling and the average of the three experiments was plotted (solid line) with the standard deviation (dashed lines).

Statistical analysis

Unless specified otherwise, statistical analysis was performed using Graphpad v7.02. The exact statistical test used for each comparison is specified in the main body of the text, together with the resulting p-values. In the case of multiple comparisons, a post-hoc analysis with Bonferroni correction was performed. Any corrected p-values derived from this post-hoc analysis are indicated in the text as p_{bon}.

Data availability

593 RNA-seq data have been deposited in the ArrayExpress database at EMBL-EBI
594 (www.ebi.ac.uk/arrayexpress) under accession number E-MTAB-10083.
595 (http://www.ebi.ac.uk/arrayexpress/experiments/E-MTAB-10083)

596 Nanotomy datasets are open access available via the repository website
597 www.nanotomy.org/PW/temp02/EllenNollen.

598 ***[to be deleted] Upon acceptance of this work the data will be open access available, without***
599 ***password. Pending acceptance, the website can only be accessed by collaborators and reviewers***

600

601 **Acknowledgments**

602 All LCOs were kindly provided by K. Peter R. Nilsson, Linköping University, Sweden. Part of the
603 work has been performed in the UMCG Microscopy and Imaging Center (UMIC), sponsored by
604 ZonMW grant 91111.006 and NWO 40-00506-98-9021. We thank Ben Giepmans for advise on EM
605 studies. This project was funded by a Meervoud Grant from NWO (836.09.001) (to E.A.A.N.), a
606 European Research Council (ERC) starting grant (281622 PDControl) (to E.A.A.N.), the Alumni
607 chapter Gooische Groningers facilitated by the Ubbo Emmius Fonds (to E.A.A.N), an Aspasia
608 fellowship from NWO (015.014.005) (to E.A.A.N.).

609 **Author Contributions**

610 E.S., O.S., L.J. and E.A.A. conceptualized the project. E.S., L.J., O.S. and W.H. performed initial
611 sample collection, sample processing and validation experiments verifying the Serf2 KO models and
612 controls. M.K., L.H., S.A.Y. and A.d.B. provided the embryonic morphological and histological
613 assessment. N.B. and M.J. provided the LCO staining and confocal imaging. A.H.G.W. performed the
614 large-scale STEM imaging. B.B. and F.F. provided assistance in the isolation and RNA seq analysis of
615 the MEFs. A.T. performed western blotting and ELISA measurements for APP and Aβ content.

616 B.v.d.S. and J.v.D. generated the initial Serf2KO animals. L.J. performed the data analysis and wrote

617 the manuscript in collaboration with E.S. and E.A.A.

618

619 **Conflict of Interests**

620 The authors declare that they have no conflict of interest.

621 **References**

622 1. Glenner, G. G. & Wong, C. W. Alzheimer's disease: Initial report of the purification and
623 characterization of a novel cerebrovascular amyloid protein. *Biochem. Biophys. Res. Commun.*
624 (1984). doi:10.1016/S0006-291X(84)80190-4

625 2. Masters, C. L. *et al.* Amyloid plaque core protein in Alzheimer disease and Down syndrome.
626 *Proc. Natl. Acad. Sci. U. S. A.* **82**, 4245–4249 (1985).

627 3. Grundke-Iqbal, I. *et al.* Microtubule-associated protein tau. A component of Alzheimer paired
628 helical filaments. *J. Biol. Chem.* **261**, 6084–6089 (1986).

629 4. Grundke-Iqbal, I. *et al.* Abnormal phosphorylation of the microtubule-associated protein tau
630 (tau) in Alzheimer cytoskeletal pathology. *Proc. Natl. Acad. Sci. U. S. A.* **83**, 4913–4917
631 (1986).

632 5. Langley, C. H. & Charlesworth, B. *Nature © Macmillan Publishers Ltd 1997 expansion of*
633 *xenotransplantation*. (1997).

634 6. Scherzinger, E. *et al. Self-assembly of polyglutamine-containing huntingtin fragments into*
635 *amyloid-like fibrils: Implications for Huntington's disease pathology (huntingtinglutamine*
636 *repeataggregation). Medical Sciences Communicated by Max F. Perutz, Medical Research*
637 *Council* **96**, 4604–4609 (1999).

638 7. Goate, A. *et al.* Segregation of a missense mutation in the amyloid precursor protein gene with
639 familial Alzheimer's disease. *Nature* **349**, 704–706 (1991).

640 8. Chartier-Harlin, M.-C. *et al.* Early-onset Alzheimer's disease caused by mutations at codon 717
641 of the β-amyloid precursor protein gene. *Nature* **353**, 844–846 (1991).

642 9. Citron, M. *et al.* Mutation of the β-amyloid precursor protein in familial Alzheimer's disease

643 increases β-protein production. *Nature* (1992). doi:10.1038/360672a0

644 10. Eckman, C. B. *et al.* A new pathogenic mutation in the APP gene (I716V) increases the relative
645 proportion of A beta 42(43). *Hum. Mol. Genet.* **6**, 2087–9 (1997).

646 11. Murrell, J. R., Hake, A. M., Quaid, K. A., Farlow, M. R. & Ghetti, B. Early-Onset Alzheimer
647 Disease Caused by a New Mutation (V717L) in the Amyloid Precursor Protein Gene. *Arch.*
648 *Neurol.* **57**, 885 (2000).

649 12. Kumar-Singh, S. *et al.* Nonfibrillar diffuse amyloid deposition due to a gamma(42)-secretase
650 site mutation points to an essential role for N-truncated A beta(42) in Alzheimer's disease.
651 *Hum. Mol. Genet.* **9**, 2589–98 (2000).

652 13. Cruts, M. *et al.* Novel APP mutation V715A associated with presenile Alzheimer's disease in a
653 German family. *J Neurol* **250**, 1374–1375 (2003).

654 14. Kumar-Singh, S. *et al.* Mean age-of-onset of familial Alzheimer disease caused by presenilin
655 mutations correlates with both increased Aβ42 and decreased Aβ40. *Hum. Mutat.* (2006).
656 doi:10.1002/humu.20336

657 15. Tomiyama, T. *et al.* A new amyloid β variant favoring oligomerization in Alzheimer's-type
658 dementia. *Ann. Neurol.* **63**, 377–387 (2008).

659 16. Schellenberg, G. *et al.* Genetic linkage evidence for a familial Alzheimer's disease locus on
660 chromosome 14. *Science (80-.).* **258**, 668–671 (1992).

661 17. Sherrington, R. *et al.* Cloning of a gene bearing missense mutations in early-onset familial
662 Alzheimer's disease. *Nature* **375**, 754–760 (1995).

663 18. Borchelt, D. R. *et al.* Familial Alzheimer's disease-linked presenilin I variants elevate aβ1-
664 42/1-40 ratio in vitro and in vivo. *Neuron* (1996). doi:10.1016/S0896-6273(00)80230-5

19. Lemere, C. A. *et al.* The E280A presenilin 1 Alzheimer mutation produces increased A beta 42 deposition and severe cerebellar pathology. *Nat. Med.* **2**, 1146–50 (1996).

20. Guerreiro, R. J. *et al.* Genetic screening of Alzheimer's disease genes in Iberian and African samples yields novel mutations in presenilins and APP. *Neurobiol. Aging* **31**, 725–731 (2010).

21. Rogaev, E. I. *et al.* Familial Alzheimer's disease in kindreds with missense mutations in a gene on chromosome 1 related to the Alzheimer's disease type 3 gene. *Nature* **376**, 775–778 (1995).

22. Citron, M. *et al.* Mutant presenilins of Alzheimer's disease increase production of 42-residue amyloid beta-protein in both transfected cells and transgenic mice. *Nat. Med.* **3**, 67–72 (1997).

23. Müller, U., Winter, P., Bolender, C. & Nolte, D. Previously Unrecognized Missense Mutation E126K of PSEN2 Segregates with Early Onset Alzheimer's Disease in a Family. *J. Alzheimer's Dis.* **42**, 109–113 (2014).

24. Haass, C. *et al.* The Swedish mutation causes early-onset Alzheimer's disease by beta-secretase cleavage within the secretory pathway. *Nat. Med.* **1**, 1291–6 (1995).

25. Suzuki, N. *et al.* An increased percentage of long amyloid β protein secreted by familial amyloid β protein precursor (βAPP717) mutants. *Science (80-.).* (1994). doi:10.1126/science.8191290

26. Duff, K. *et al.* Increased amyloid-β42(43) in brains of mice expressing mutant presenilin 1. *Nature* (1996). doi:10.1038/383710a0

27. Murayama, O. *et al.* Enhancement of amyloid β 42 secretion by 28 different presenilin 1 mutations of familial Alzheimer's disease. *Neurosci. Lett.* **265**, 61–63 (1999).

28. Nilsberth, C. *et al.* The 'Arctic' APP mutation (E693G) causes Alzheimer's disease by enhanced Aβ protofibril formation. *Nat. Neurosci.* **4**, 887–893 (2001).

687 29. Miravalle, L. *et al.* Substitutions at Codon 22 of Alzheimer's A Peptide Induce Diverse
688 Conformational Changes and Apoptotic Effects in Human Cerebral Endothelial Cells*. (2000).
689 doi:10.1074/jbc.M003154200

690 30. Ni, C.-L., Shi, H.-P., Yu, H.-M., Chang, Y.-C. & Chen, Y.-R. Folding stability of amyloid-β 40
691 monomer is an important determinant of the nucleation kinetics in fibrillization. *FASEB J.* **25**,
692 1390–1401 (2011).

693 31. Conway, K. A., Harper, J. D. & Lansbury, P. T. Accelerated in vitro fibril formation by a
694 mutant α-synuclein linked to early-onset Parkinson disease. *Nat. Med.* (1998).
695 doi:10.1038/3311

696 32. Narhi, L. *et al.* Both Familial Parkinson's Disease Mutations Accelerate α-Synuclein
697 Aggregation. *J. Biol. Chem.* **274**, 9843–9846 (1999).

698 33. Conway, K. A. *et al.* Acceleration of oligomerization, not fibrillization, is a shared property of
699 both α-synuclein mutations linked to early-onset Parkinson's disease: Implications for
700 pathogenesis and therapy. *Proc. Natl. Acad. Sci. U. S. A.* (2000). doi:10.1073/pnas.97.2.571

701 34. Ghosh, D. *et al.* The Parkinson's Disease-Associated H50Q Mutation Accelerates α-Synuclein
702 Aggregation *in Vitro*. *Biochemistry* **52**, 6925–6927 (2013).

703 35. Ghosh, D. *et al.* The Newly Discovered Parkinson's Disease Associated Finnish Mutation
704 (A53E) Attenuates α-Synuclein Aggregation and Membrane Binding. *Biochemistry* **53**, 6419–
705 6421 (2014).

706 36. Choi, W. *et al.* Mutation E46K increases phospholipid binding and assembly into filaments of
707 human α-synuclein. *FEBS Lett.* **576**, 363–368 (2004).

708 37. Cooper, J. K. *et al.* Truncated N-terminal fragments of huntingtin with expanded glutamine
709 repeats form nuclear and cytoplasmic aggregates in cell culture. *Hum. Mol. Genet.* (1998).

710 doi:10.1093/hmg/7.5.783

711 38. Nekooki-Machida, Y. *et al.* Distinct conformations of in vitro and in vivo amyloids of
712 huntingtin-exon1 show different cytotoxicity. *Proc. Natl. Acad. Sci. U. S. A.* **106**, 9679–84
713 (2009).

714 39. Sun, C.-S. *et al.* Conformational switch of polyglutamine-expanded huntingtin into benign
715 aggregates leads to neuroprotective effect. *Sci. Rep.* **5**, 14992 (2015).

716 40. Cohen, M. L. *et al.* Rapidly progressive Alzheimer's disease features distinct structures of
717 amyloid-β. *Brain* **138**, 1009–1022 (2015).

718 41. Qiang, W., Yau, W.-M., Lu, J.-X., Collinge, J. & Tycko, R. Structural variation in amyloid-β
719 fibrils from Alzheimer's disease clinical subtypes. *Nature* **541**, 217–221 (2017).

720 42. Bousset, L. *et al.* Structural and functional characterization of two alpha-synuclein strains. *Nat.*
721 *Commun.* **4**, 2575 (2013).

722 43. Heise, H. *et al.* Solid-State NMR Reveals Structural Differences between Fibrils of Wild-Type
723 and Disease-Related A53T Mutant α-Synuclein. *J. Mol. Biol.* **380**, 444–450 (2008).

724 44. Li, B. *et al.* Cryo-EM of full-length α-synuclein reveals fibril polymorphs with a common
725 structural kernel. *Nat. Commun.* **9**, 3609 (2018).

726 45. Guerrero-Ferreira, R. *et al.* Two new polymorphic structures of alpha-synuclein solved by
727 cryo-electron microscopy. *bioRxiv* 654582 (2019). doi:10.1101/654582

728 46. Gath, J. *et al.* Unlike Twins: An NMR Comparison of Two α-Synuclein Polymorphs Featuring
729 Different Toxicity. *PLoS One* **9**, e90659 (2014).

730 47. Cohen, E. *et al.* Reduced IGF-1 Signaling Delays Age-Associated Proteotoxicity in Mice. *Cell*

139, 1157–1169 (2009).

48. Lu, J. X. *et al.* Molecular structure of β-amyloid fibrils in alzheimer's disease brain tissue. *Cell* (2013). doi:10.1016/j.cell.2013.08.035

49. Rasmussen, J. *et al.* Amyloid polymorphisms constitute distinct clouds of conformational variants in different etiological subtypes of Alzheimer's disease. *Proc. Natl. Acad. Sci.* **114**, 13018–13023 (2017).

50. van Ham, T. J. *et al.* Identification of MOAG-4/SERF as a regulator of age-related proteotoxicity. *Cell* **142**, 601–612 (2010).

51. Falsone, S. F. *et al.* SERF Protein Is a Direct Modifier of Amyloid Fiber Assembly. *Cell Rep.* **2**, 358–371 (2012).

52. Yoshimura, Y. *et al.* MOAG-4 promotes the aggregation of α-synuclein by competing with self-protective electrostatic interactions. *J. Biol. Chem.* **292**, 8269–8278 (2017).

53. Merle, D. A. *et al.* Increased Aggregation Tendency of Alpha-Synuclein in a Fully Disordered Protein Complex. *J. Mol. Biol.* **431**, 2581–2598 (2019).

54. Kaufman, M. H. *The Atlas of Mouse Development*. (Elsevier Science, 1992).

55. Kaufman, M. H. & Bard, J. B. L. *The Anatomical Basis of Mouse Development*. (Elsevier Science, 1999).

56. Ward, J. M., Elmore, S. A. & Foley, J. F. Pathology Methods for the Evaluation of Embryonic and Perinatal Developmental Defects and Lethality in Genetically Engineered Mice. *Vet. Pathol.* **49**, 71–84 (2012).

57. Ciemerych, M. A. & Sicinski, P. Cell cycle in mouse development. *Oncogene* (2005).

752 doi:10.1038/sj.onc.1208608

753 58. Takashima, Y. *et al.* Neuroepithelial Cells Supply an Initial Transient Wave of MSC
754 Differentiation. *Cell* **129**, 1377–1388 (2007).

755 59. Pevny, L. H., Sockanathan, S., Placzek, M. & Lovell-Badge, R. A role for SOX1 in neural
756 determination. *Development* (1998).

757 60. Wood, H. B. & Episkopou, V. Comparative expression of the mouse Sox1, Sox2 and Sox3
758 genes from pre-gastrulation to early somite stages. *Mech. Dev.* (1999). doi:10.1016/S0925-
759 4773(99)00116-1

760 61. Radde, R. *et al.* Abeta42-driven cerebral amyloidosis in transgenic mice reveals early and
761 robust pathology. *EMBO Rep.* **7**, 940–6 (2006).

762 62. Klingstedt, T. *et al.* Synthesis of a library of oligothiophenes and their utilization as fluorescent
763 ligands for spectral assignment of protein aggregates. *Org. Biomol. Chem.* **9**, 8356–70 (2011).

764 63. Psonka-Antonczyk, K. M. *et al.* Nanoscale Structure and Spectroscopic Probing of Aβ1-40
765 Fibril Bundle Formation. *Front. Chem.* (2016). doi:10.3389/fchem.2016.00044

766 64. Nyström, S. *et al.* Evidence for Age-Dependent in Vivo Conformational Rearrangement within
767 Aβ Amyloid Deposits. *ACS Chem. Biol.* **8**, 1128–1133 (2013).

768 65. Lord, A. *et al.* Observations in APP bitransgenic mice suggest that diffuse and compact plaques
769 form via independent processes in Alzheimer's disease. *Am. J. Pathol.* **178**, 2286–2298 (2011).

770 66. Meyer, N. H. *et al.* Structural fuzziness of the RNA-organizing protein SERF1a determines a
771 toxic gain-of-interaction. *bioRxiv* 713511 (2019). doi:10.1101/713511

772 67. Murray, S. A. *et al.* Mouse Gestation Length Is Genetically Determined. *PLoS One* **5**, e12418

(2010).

68. Visintin, R. & Amon, A. The nucleolus: the magician's hat for cell cycle tricks. *Curr. Opin. Cell Biol.* **12**, 372–377 (2000).

69. Leung, A. K. L. *et al.* Quantitative kinetic analysis of nucleolar breakdown and reassembly during mitosis in live human cells. *J. Cell Biol.* **166**, 787–800 (2004).

70. Petkova, A. T. *et al.* Self-propagating, molecular-level polymorphism in Alzheimer's β-amyloid fibrils. *Science (80-.).* (2005). doi:10.1126/science.1105850

71. Meinen, B. A., Gadkari, V. V., Stull, F., Ruotolo, B. T. & Bardwell, J. C. A. SERF engages in a fuzzy complex that accelerates primary nucleation of amyloid proteins. *Proc. Natl. Acad. Sci.* (2019). doi:10.1073/pnas.1913316116

72. Pras, A. *et al.* The cellular modifier MOAG-4/SERF drives amyloid formation through charge complementation. *bioRxiv* 2020.12.09.417709 (2020). doi:10.1101/2020.12.09.417709

73. Grant, M. A. *et al. Familial Alzheimer's disease mutations alter the stability of the amyloid-protein monomer folding nucleus*. **104**, (2007).

74. Lazo, N. D., Grant, M. A., Condron, M. C., Rigby, A. C. & Teplow, D. B. On the nucleation of amyloid β-protein monomer folding. *Protein Sci.* **14**, 1581–1596 (2009).

75. Elkins, M. R. *et al.* Structural Polymorphism of Alzheimer's β-Amyloid Fibrils as Controlled by an E22 Switch: A Solid-State NMR Study. (2016). doi:10.1021/jacs.6b03715

76. Ovchinnikova, O. Y., Finder, V. H., Vodopivec, I., Nitsch, R. M. & Glockshuber, R. The Osaka FAD Mutation E22Δ Leads to the Formation of a Previously Unknown Type of Amyloid β Fibrils and Modulates Aβ Neurotoxicity. *J. Mol. Biol.* **408**, 780–791 (2011).

794 77. Van Nostrand, W. E., Melchor, J. P., Cho, H. S., Greenberg, S. M. & Rebeck, G. W.
795 Pathogenic effects of D23N Iowa mutant amyloid beta -protein. *J. Biol. Chem.* **276**, 32860–6
796 (2001).

797 78. Inayathullah, M. & Teplow, D. B. Structural dynamics of the Δe22 (Osaka) familial
798 Alzheimer's disease-linked amyloid β-protein. *Amyloid* **18**, 98–107 (2011).

799 79. Bugiani, O. *et al.* Hereditary Cerebral Hemorrhage With Amyloidosis Associated With the
800 E693K Mutation of APP. *Arch. Neurol.* **67**, 987–995 (2010).

801 80. Grabowski, T. J., Cho, H. S., Vonsattel, J. P. G., Rebeck, G. W. & Greenberg, S. M. Novel
802 amyloid precursor protein mutation in an Iowa family with dementia and severe cerebral
803 amyloid angiopathy. *Ann. Neurol.* **49**, 697–705 (2001).

804 81. Philipson, O. *et al.* A highly insoluble state of Aβ similar to that of Alzheimer's disease brain is
805 found in Arctic APP transgenic mice. *Neurobiol. Aging* **30**, 1393–1405 (2009).

806 82. Shimada, H. *et al.* Clinical course of patients with familial early-onset Alzheimer's disease
807 potentially lacking senile plaques bearing the E693Δ mutation in amyloid precursor protein.
808 *Dement. Geriatr. Cogn. Disord.* **32**, 45–54 (2011).

809 83. Tomiyama, T. *et al.* A Mouse Model of Amyloid β Oligomers: Their Contribution to Synaptic
810 Alteration, Abnormal Tau Phosphorylation, Glial Activation, and Neuronal Loss In Vivo. *J.*
811 *Neurosci.* **30**, 4845–4856 (2010).

812 84. Lord, A. *et al.* The Arctic Alzheimer mutation facilitates early intraneuronal Aβ aggregation
813 and senile plaque formation in transgenic mice. *Neurobiol. Aging* **27**, 67–77 (2006).

814 85. Kulic, L. *et al.* Early accumulation of intracellular fibrillar oligomers and late congophilic
815 amyloid angiopathy in mice expressing the Osaka intra-Aβ APP mutation. *Transl. Psychiatry*
816 **2**, e183–e183 (2012).

817 86. Philipson, O. *et al.* The Arctic amyloid-β precursor protein (AβPP) mutation results in distinct
818 plaques and accumulation of N- and C-truncated Aβ. *Neurobiol. Aging* **33**, 1010.e1-1010.e13
819 (2012).

820 87. Skarnes, W. C. *et al.* A conditional knockout resource for the genome-wide study of mouse
821 gene function. *Nature* **474**, 337–342 (2011).

822 88. Huang, D. W., Sherman, B. T. & Lempicki, R. A. Systematic and integrative analysis of large
823 gene lists using DAVID bioinformatics resources. *Nat. Protoc.* **4**, 44–57 (2009).

824 89. Huang, D. W., Sherman, B. T. & Lempicki, R. A. Bioinformatics enrichment tools: paths
825 toward the comprehensive functional analysis of large gene lists. *Nucleic Acids Res.* **37**, 1–13
826 (2009).

827 90. Huang, Y. *et al.* Loss of GPR3 reduces the amyloid plaque burden and improves memory in
828 Alzheimer's disease mouse models. *Sci. Transl. Med.* **7**, 309ra164 (2015).

829 91. Schindelin, J. *et al.* Fiji: an open-source platform for biological-image analysis. *Nat. Methods*
830 **9**, 676–682 (2012).

831

Figure legends

Figure 1. Full-body *Serf2*$^{-/-}$ mice display a developmental delay and perinatal lethality. (A) Schematic overview of the crossing scheme with full-body *Serf2*$^{+/-}$ mice and the resulting genotypic composition of the offspring at embryonic and postnatal stage. **(B)** Absolute animal counts for the three genotypes in the offspring at various days of embryonic development(E13.5, E15.5 and E17.5), at birth (P0) and at time of weaning (P22). **(C)** Real time RT-PCR analyses of *Serf1* and *Serf2* RNA levels in E13.5 heads normalized to housekeeping gene beta-actin (n=4/group, mean±SD, One-way ANOVA for each gene, Bonferroni corrected post-hoc comparison between genotypes ***p<0.001). **(D)** Western blot of SERF2 and actin in *Serf2*$^{+/+}$, *Serf2*$^{+/-}$, *Serf2*$^{-/-}$embryos at E13.5 (black arrow indicates SERF2 band). **(E)** Length measurements of *Serf2*$^{+/+}$, *Serf2*$^{+/-}$, *Serf2*$^{-/-}$ embryos at E15.5, E17.5 and P0 (black line = mean, Two-way ANOVA with factors age and genotype, Bonferroni corrected post-hoc comparison for *Serf2*$^{+/-}$ and *Serf2*$^{-/-}$ compared to *Serf2*$^{-/-}$ *p<0.05; ***p<0.001). **(F)** Hematoxylin and eosin stained lung tissue from *Serf2*$^{+/+}$ and *Serf2*$^{-/-}$ pups at P0 (top: *Serf2*$^{-/-}$, bottom: *Serf2*$^{+/+}$, scale bar=500µm, rectangle =5x magnification in right picture, **(G)** Quantification of the saccolar space in lung tissue from *Serf2*$^{+/+}$ and *Serf2*$^{-/-}$ pups at P0 (black line = mean, t-test **p<0.01). For all mouse data panels: *Serf2*$^{+/+}$= black, *Serf2*$^{+/-}$ = dark grey, *Serf2*$^{-/-}$ = light grey.

Figure 2. Crossing a conditional *Serf2* KO with an AM background does not affect the overall levels of APP and Aβ. (A) Schematic overview of the cross between brain-specific *Serf2* KO mice and the amyloid model resulting in four experimental groups: WT, *Serf2*$^{br-/-}$, AM and AM;*Serf2*$^{br-/-}$. **(B)** Timeline for the Aβ pathology in the amyloid model and the selected time points for this study. **(C)** Real time RT-PCR analyses of *Serf2* RNA levels in the brain tissue of all experimental groups at 1 and 3 months of age normalized to housekeeping gene beta-actin (n=6/group, mean±SD, Two-way ANOVA with factors age and genotype, Bonferroni corrected post-hoc for individual groups compared to WT). **(D)** Western blot of SERF2 and actin in brain tissue of all experimental groups at 1 and 3 months of age. **(E)** Brain weight of all experimental groups at 1 and 3 months of age (black line = mean, Two-way ANOVA with factors age and genotype, Bonferroni corrected post-hoc for

858 individual groups compared to WT). **(F)** Brain weight of unfloxed control groups at 3 months of age
859 (black line = mean, One-way ANOVA, Bonferroni corrected post-hoc for individual groups compared
860 to WT). **(G)** Number of cortical nuclei per mm^2 in hematoxylin and eosin stained brain tissue of all
861 experimental groups at 3 months of age. (n=3/group, mean±SD, Kruskal-Wallis p=0.5566). **(H)** Real
862 time RT-PCR analyses of APP RNA levels in the brain tissue of AM and AM;*Serf2*$^{br-/-}$ mice at 1 and 3
863 months of age normalized to housekeeping gene beta-actin (n=6/group, mean±SD, t-test between
864 genotypes at both ages not significant). **(I)** Western blot of APP and beta-actin in brain tissue of AM
865 and AM;*Serf2*$^{br-/-}$ mice at 3 months of age versus 1-month-old non-AM controls. **(J)** Quantification of
866 total APP protein levels in brains of AM and AM;*Serf2*$^{br-/-}$ mice at 1 and 3 months of age normalized
867 to beta-actin levels. (black line = mean, t-test between genotypes at both ages not significant). **(K)**
868 $A\beta_{40}$ and **(L)** $A\beta_{42}$ levels in brain lysate from AM and AM;*Serf2*$^{br-/-}$ mice at 1 and 3 months of age as
869 determined by ELISA normalized to total protein content. (black line = mean, t-test between
870 genotypes at both ages not significant). **(M)** Correlation plot depicting the relationship between $A\beta_{40}$
871 and $A\beta_{42}$ levels in AM (black) and AM;*Serf2*$^{br-/-}$ (grey) mice at 3 months of age (detailed statistics in
872 Supplemental Table 3). In panels A-L: WT = black, *Serf2*$^{br-/-}$ = light grey , AM = dark grey and
873 AM;*Serf2*$^{br-/-}$ = white; ***p<0.001; **p<0.01.

874 **Figure 3. Brain-specific *Serf2* KO display increased Aβ deposition and amyloid .(A)** Detailed light
875 microscope images of the 6E10-stained cortical region marked on the sagittal section in Supplemental
876 Figure 5 from 3-month-old AM and AM;*Serf2*$^{br-/-}$ mice (scale bar = 100μm). **(B)** Quantification of the
877 Aβ deposits in the region of interest (ROI) of 6E10 immunostained sagittal brain sections from 1- and
878 3-month-old AM and AM;*Serf2*$^{br-/-}$ mice (black line = mean, One-way ANOVA between genotypes at
879 both ages, Bonferroni corrected post-hoc between AM and AM;*Serf2*$^{br-/-}$ not significant). **(C)**
880 Correlation plot depicting the relationship between $A\beta_{40}$ levels and 6E10 plaque density in AM (black)
881 and AM;*Serf2*$^{br-/-}$ (grey) mice at 3 months of age. **(D)** Correlation plot depicting the relationship
882 between $A\beta_{42}$ levels and 6E10 plaque density in AM (black) and AM;*Serf2*$^{br-/-}$ (grey) mice at 3 months
883 of age. **(E)** Quantification of the Aβ deposits in the ROI of W0-2 immunostained sagittal brain
884 sections from 1- and 3-month-old AM and AM;*Serf2*$^{br-/-}$ mice (black line = mean, One-way ANOVA

between genotypes at both ages, Bonferroni corrected post-hoc between AM and AM;*Serf2*$^{br-/-}$ not significant). **(F)** Correlation plot depicting the relationship between 6E10 deposits and W0-2 deposits in AM (black) and AM;*Serf2*$^{br-/-}$ (grey) mice at 3 months of age. **(G)** Quantification of the plaque density in the ROI of Thioflavin-S stained sagittal brain sections from 1- and 3-month-old AM and AM;*Serf2*$^{br-/-}$ mice (black line = mean, One-way ANOVA between genotypes at both ages, Bonferroni corrected post-hoc between AM and AM;*Serf2*$^{br-/-}$ not significant). **(H)** Correlation plot depicting the relationship between $A\beta_{40}$ levels and ThS plaque density in AM (black) and AM;*Serf2*$^{br-/-}$ (grey) mice at 3 months of age. **(I)** Correlation plot depicting the relationship between $A\beta_{42}$ levels and ThS plaque density in AM (black) and AM;*Serf2*$^{br-/-}$ (grey) mice at 3 months of age. **(I)** Correlation plot depicting the relationship between 6E10 deposits and ThS plaques in AM (black) and AM;*Serf2*$^{br-/-}$ (grey) mice at 3 months of age. In all panels ROI = cortical and hippocampal area; In panels B,E and G: WT = black, *Serf2*$^{br-/-}$ = light grey , AM = dark grey and AM;*Serf2*$^{br-/-}$ = white; for correlation plots: detailed statistics in Supplemental Table 3; ***p<0.001; **p<0.01; *p <0.05.

Figure 4. Brain-specific *Serf2* KO alters the structural composition of amyloid plaques. (A) Graph showing the theoretical LCO dye emission spectra for qFTAA, which binds mature Aβ fibrils (blue), and hFTAA, which binds both mature fibrils and prefibrillar Aβ species (red). **(B)** Frequency distribution of the ratio in fluorescence intensity at 502 nm and 588 nm for all amyloid plaques identified by confocal microscopy in AM (blue) and AM;*Serf2*$^{br-/-}$ (red) mice at 3 months of age. Three peak frequency categories were identified: low IR(red), medium IR (green) and high IR (blue) (n=6 mice/genotype). **(C)** Dot plot representing the intensity ratio of all amyloid plaques identified by confocal microscopy for AM and AM;*Serf2*$^{br-/-}$ mice at 3 months of age (colors represent the IR categories defined in panel B, black circles correspond to the plaques depicted in panel E, black line = mean, t-test ***p<0.001) (n=6 mice/genotype). **(D)** Correlation plot depicting the relationship between 6E10 plaque density in the ROI and the LCO average intensity ratio in AM (black) and AM;*Serf2*$^{br-/-}$ (grey) mice at 3 months of age (ROI = cortical and hippocampal area, detailed statistics in Supplemental Table 3). **(E)** Spectral confocal microscopy images of amyloid plaques in AM and AM;*Serf2*$^{br-/-}$ mice at 3 months of age of double stained with qFTAA and hFTAA (top= fluorescence

912 at 502 nm, middle= fluorescence at 588 nm, bottom=merged image of 502 nm and 588 nm
913 fluorescence, scale bar = 5 μm). **(F)** Scanning transmission electron microscopy pictures of amyloid
914 plaques in the cortex of AM and AM;*Serf2*$^{br-/-}$ mice at 3 months of age (top scale bar 5μm, rectangle =
915 zoomed region in bottom picture, bottom scale bar = 1μm). High-resolution EM images are available
916 via http://www.nanotomy.org.

Figure 1

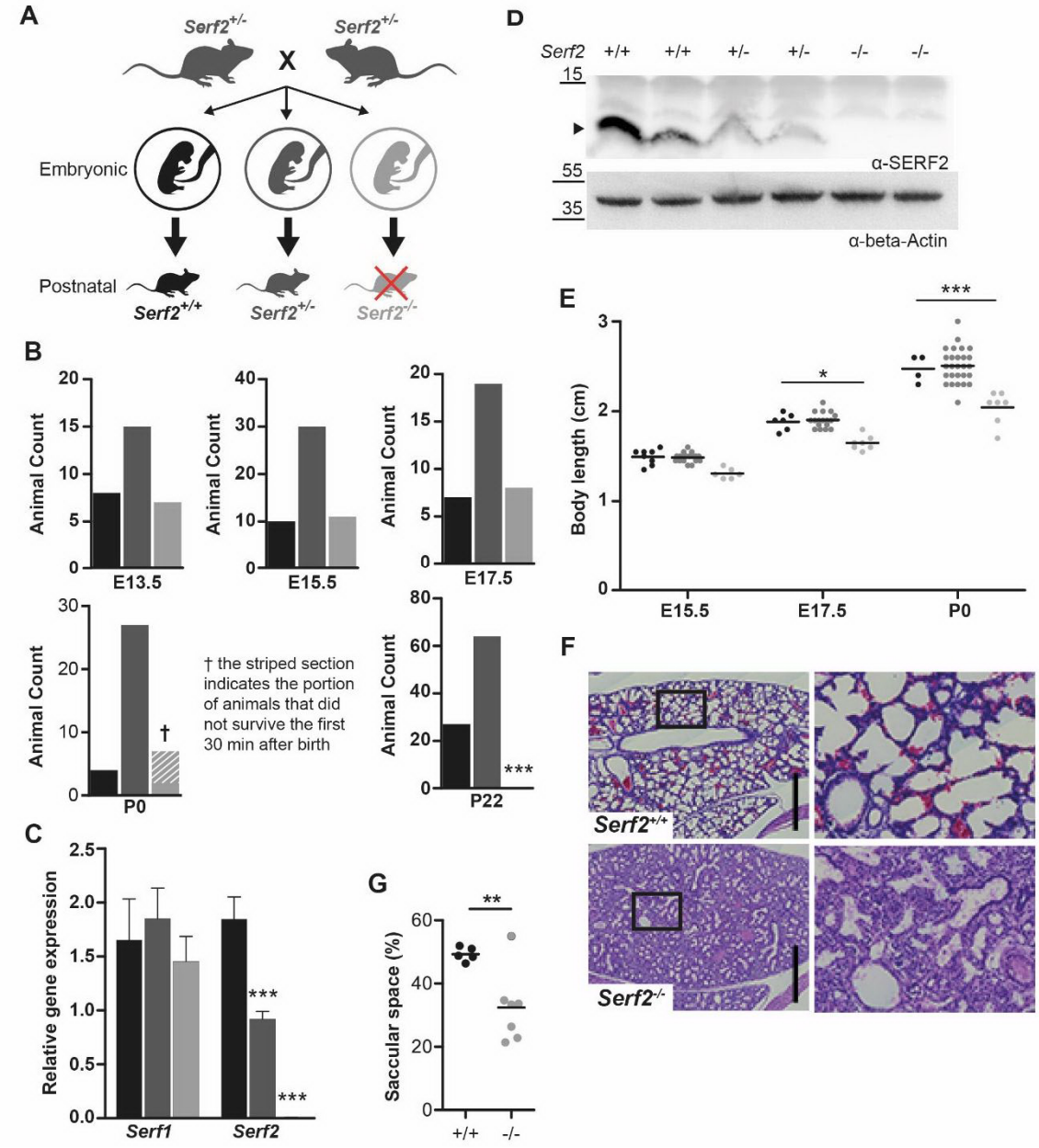

917

Figure 2

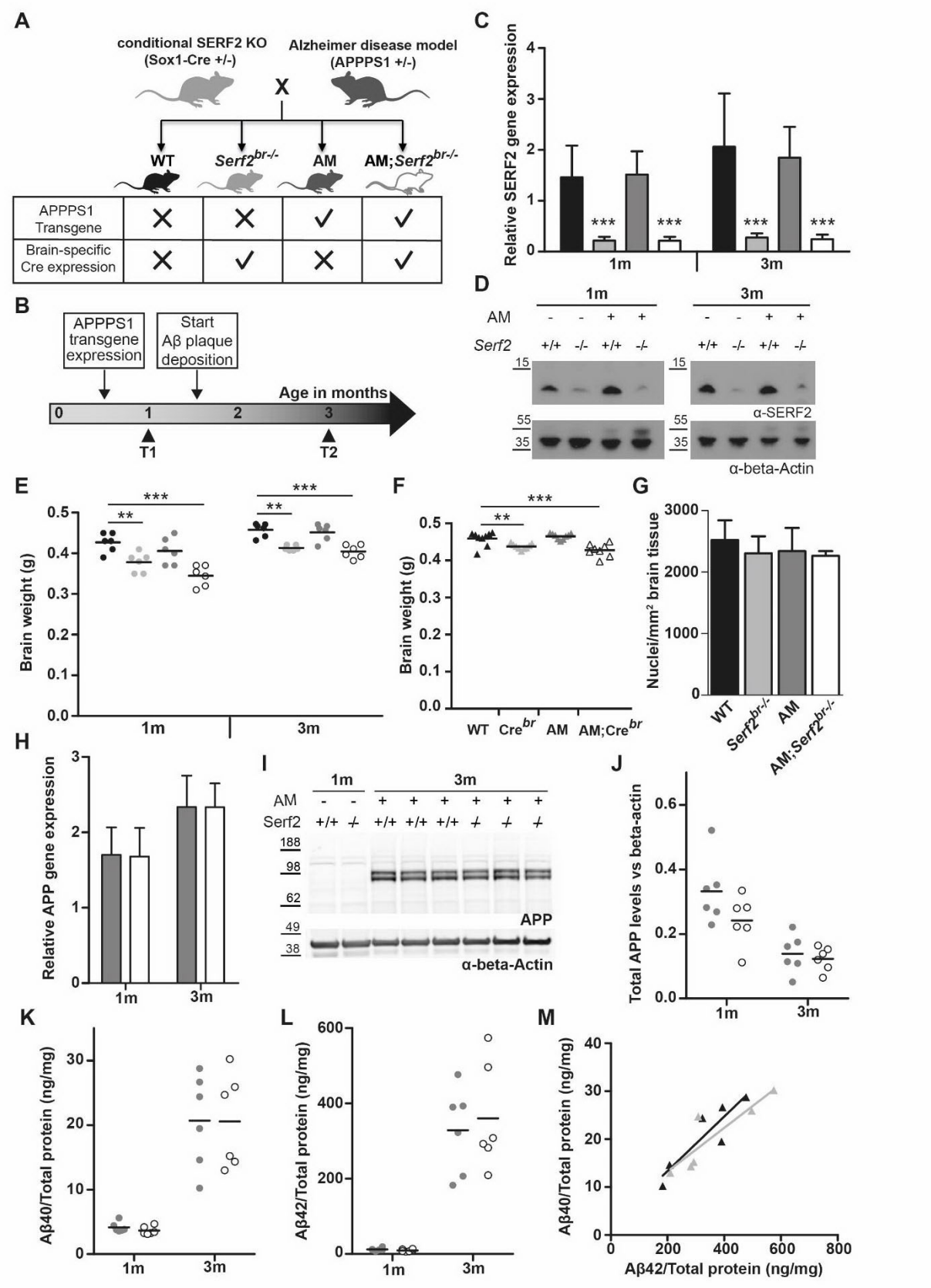

Figure 3

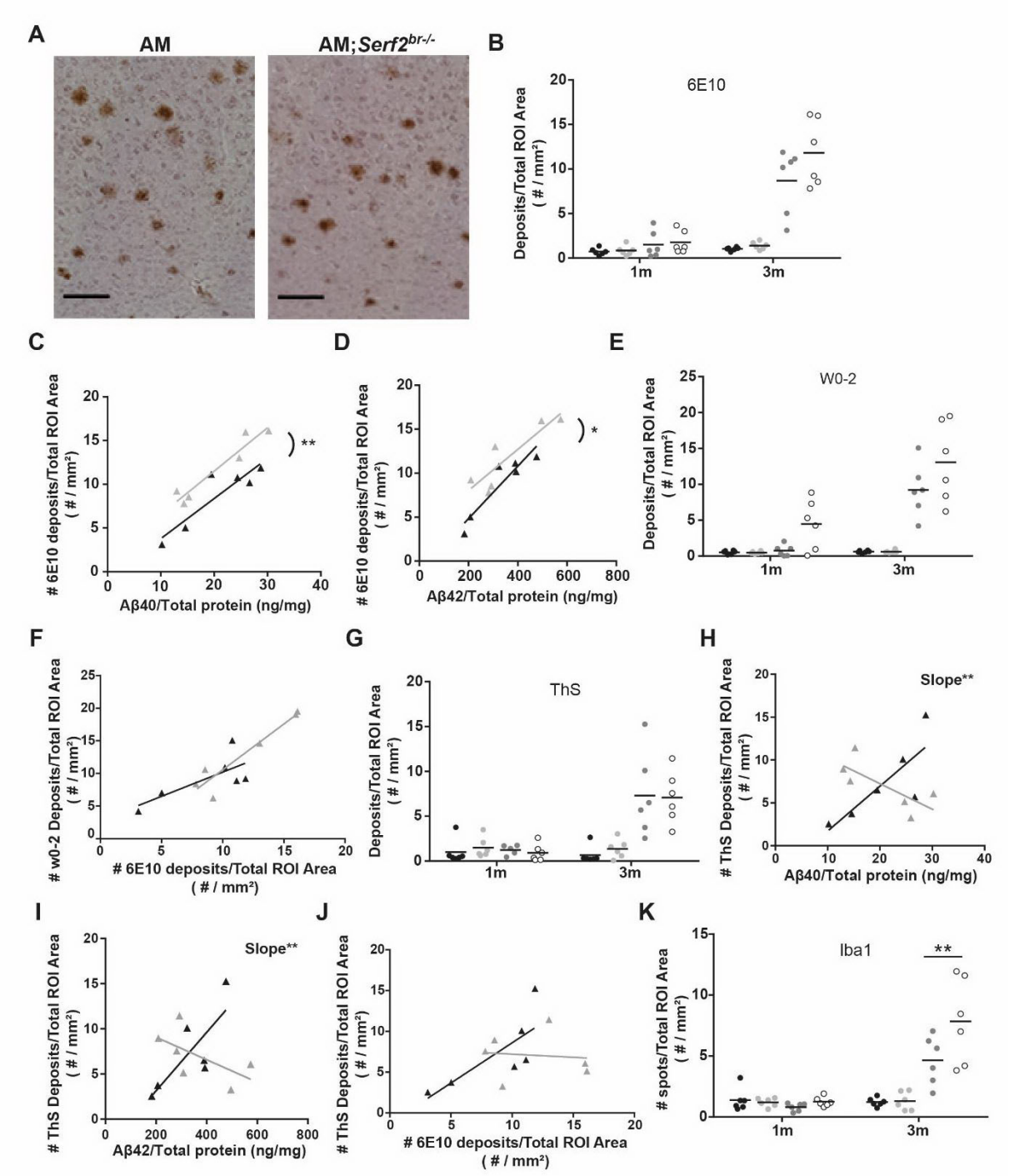

Figure 4

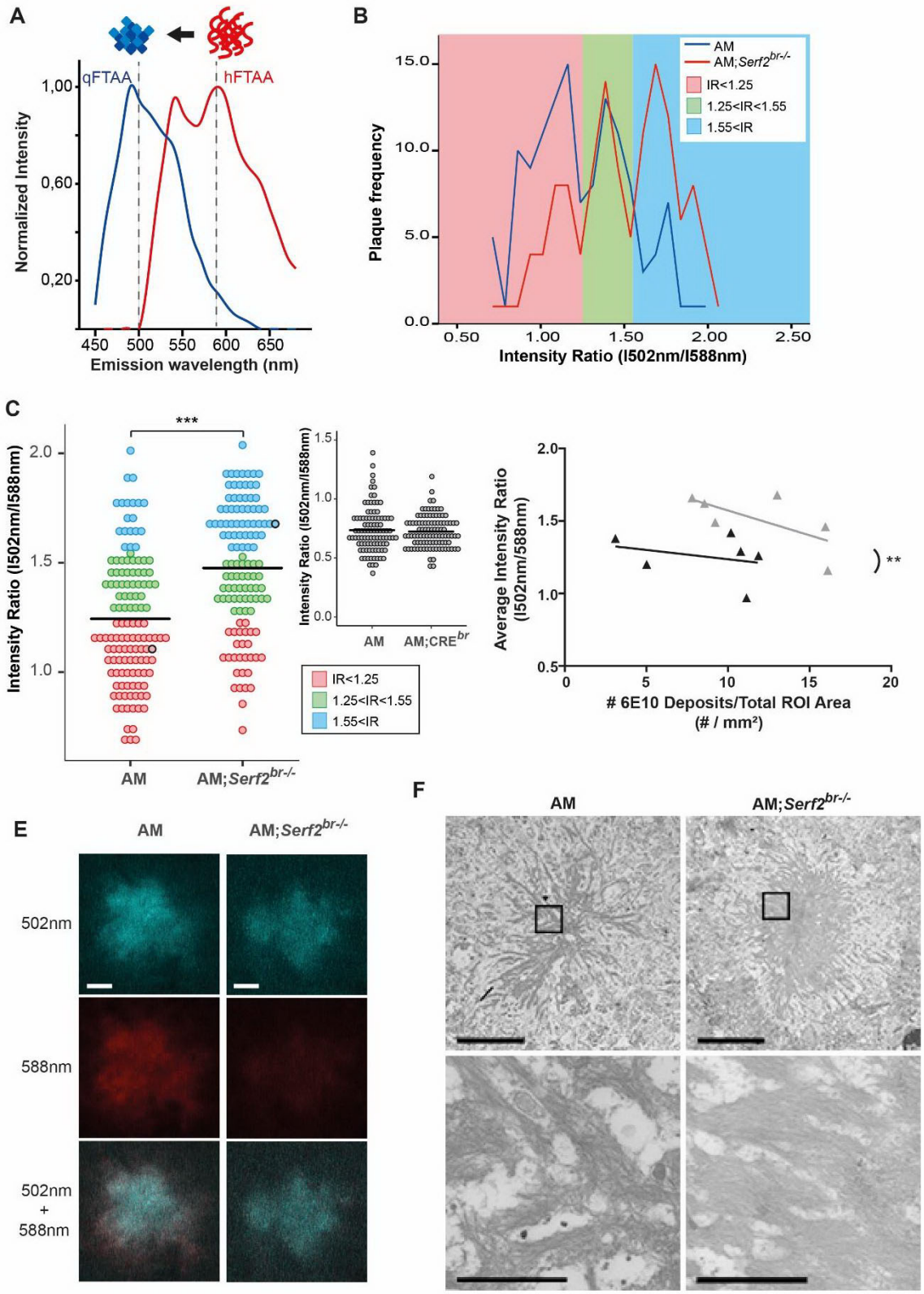

Supplemental figure legends

Supplemental Figure 1. Additional full-body *Serf2*$^{-/-}$ mice validation and phenotype confirmation. (A) Targeting strategy used to delete exon 2 of *Serf2* by using the 'knockout-first'-allele (adjusted from Skarnes et al. 2011). Top panel: exon/intron structure of *Serf2* including the positions of the LacZ and Neo cassettes, as well as loxP sites. Bottom panel: the *Serf2* allele after recombination events as a result of crosses with *Hprt-Cre* mice. **(B)** Western blot analysis of liver, heart and brain tissue of a *Serf2*$^{+/+}$, *Serf2*$^{+/-}$ and *Serf2*$^{-/-}$ adult mice to detect Serf2 and actin. **(C)** Real time RT-PCR analyses of *Serf2* in different organs of adult mice with the following genotypes *Serf2*$^{+/+}$ (n=3), *Serf2*$^{+/-}$ (n=8) and *Serf2*$^{-/-}$ (n=1). *Serf2* levels were normalized to the housekeeping gene 18S (mean ± SEM). **(D)** Lateral view of a *Serf2*$^{-/-}$ and *Serf2*$^{+/-}$ embryo and placenta at embryonic day 15.5 and 17.5. **(E)** Weight measurements of *Serf2*$^{+/+}$, *Serf2*$^{+/-}$, *Serf2*$^{-/-}$ embryos at E17.5 and P0 (black line = mean, Two-way ANOVA with factors age and genotype, Bonferroni corrected post-hoc comparison for *Serf2*$^{+/-}$ and *Serf2*$^{-/-}$ compared to *Serf2*$^{-/-}$ *p<0.05; ***p<0.001). **(F)** Hematoxylin and Eosin staining on *Serf2*$^{-/-}$ and *Serf2*$^{+/+}$ lung and kidney tissue at E17.5 (10 times magnification). For all panels: *Serf2*$^{+/+}$= black, *Serf2*$^{+/-}$ = dark grey, *Serf2*$^{-/-}$ = light grey.

Supplemental Figure 2. Cell culture data of *Serf2* KO and control HEK cells and RNA sequencing analysis of mouse embryonic fibroblasts (MEFs) isolated from full-body *Serf2*$^{-/-}$ and control mice. (A) Growth curve of two CRISPR-induced *Serf2*$^{-/-}$ clones of HEK293T versus wild-type HEK293T. (Three replicates measured,full line=replicate average, dashed lines=standard deviation on average) **(B)** Network showing the interconnectivity of enriched GO-terms in RNA sequencing data from *Serf2*$^{-/-}$ and control MEFs. Circle size indicates amount of differentially expressed genes found in each GO-category. Edges were drawn when the minor category shared more than 25 % of its found genes with the major category. Edge color indicates the major category in the relationship. Edge thickness indicates the percentage of found genes shared by the minor category. **(C)** Bar chart indicating the fold change for each GO-term as determined by DAVID. Brackets indicate the three main GO-term clusters defined based on the network in (B).

Supplemental Figure 3. Additional validation of the brain-specific knock-out of *Serf2*. (A) Modified targeting strategy used to delete the exon 2 of *Serf2* specifically in the central nervous system. **(B)** Real time RT-PCR analyses of *Serf2* RNA expression in different organs $Serf2^{+/+}$ and $Serf2^{br-/-}$ female mice at 1 month and 3 months of age. *Serf2* expression was normalized to housekeeping gene beta-actin (all groups n=6, mean ± SEM). **(C)** Western blot analysis and quantification of *Serf2* and beta-actin in brain lysates of WT and $Serf2^{br-/-}$ female mice at 1 month (both groups n=6, mean ± SEM, t-test **p<0.01). **(D)** Brain weight of unfloxed WT and CRE^{br} mice at 1 and 3 months of age (black line = mean, Two-way ANOVA with factors age and genotype, Bonferroni corrected post-hoc for CRE^{br} compared to WT *p_{bon}<0.05). **(E)** Evolution of brain weight in WT and $Serf2^{br-/-}$ female mice between 1 and 11 months of age (black line = mean).

Supplemental Figure 4. Overview of distribution and general morphological parameters of 6E10-stained Aβ deposits in AM and AM;$Serf2^{br-/-}$ mice at 3 months of age. (A) Light microscope images of the 6E10 immunostained sagittal section of 3-month-old AM and AM;$Serf2^{br-/-}$ female mice (scale bar = 1mm, black rectangle = magnified region in main Figure 3). **(B)** Boxplots showing the distribution of the surface area of the individual plaques measured in AM and AM;$Serf2^{br-/-}$ mice at 3 months of age. **(C)** Boxplots showing the distribution of the circularity of the individual plaques measured in AM and AM;$Serf2^{br-/-}$ mice at 3 months of age. **(D)** Boxplots showing the distribution of the solidity of the individual plaques measured in AM and AM;$Serf2^{br-/-}$ mice at 3 months of age. For all boxplots: black line = median, box = 25^{th}-75^{th} percentile, whiskers = 1.5 x interquartile range (IQR), circles = outlier value > 1.5x IQR, asterisks = extreme outlier value > 3x IQR.

Supplemental Figure 5. Overview of distribution and detailed W0-2-stained Aβ deposits in AM and AM;$Serf2^{br-/-}$ mice at 3 months of age. Light microscope images of the W0-2 immunostained sagittal section of 3-month-old AM and AM;$Serf2^{br-/-}$ female mice (scale bar = 1mm, black rectangle = magnified in insert on the right, insert scale bar = 100µm).

Supplemental Figure 6. Correlation plots illustrating the relationship of different stains in individual mice. (A) Correlation plot depicting the relationship between the density of 6E10 deposits

969 and Iba1-positive spots in AM (black) and AM;*Serf2*$^{br-/-}$ (grey) mice at 3 months of age. **(B)**
970 Correlation plot depicting the relationship between W0-2 plaque density and the LCO average
971 intensity ratio in AM (black) and AM;*Serf2*$^{br-/-}$ (grey) mice at 3 months of age. **(C)** Correlation plot
972 depicting the relationship between ThS plaque density and the LCO average intensity ratio in AM
973 (black) and AM;*Serf2*$^{br-/-}$ (grey) mice at 3 months of age. For all plots: detailed statistics in
974 Supplemental Table 3; *p <0.05.

975 **Supplemental Figure 7. Overview and detailed view of Aβ staining pattern after W0-2 and 6E10**
976 **staining in AM and AM;*Serf2*$^{br-/-}$ mice at 1 month of age. (A)** Light microscope images of the W0-2
977 immunostained sagittal section of 1-month-old AM and AM;*Serf2*$^{br-/-}$ female mice. **(B)** Light
978 microscope images of the 6E10 immunostained sagittal section of 1-month-old AM and AM;*Serf2*$^{br-/-}$
979 female mice. All pictures: main scale bar = 1mm, black rectangle = magnified in insert on the right,
980 insert scale bar = 100µm.